

# Chemical Science

Accepted Manuscript

This article can be cited before page numbers have been issued, to do this please use: J. L. Lee, S. Saeed and J. M. Mayer, *Chem. Sci.*, 2026, DOI: 10.1039/D6SC00492J.



This is an Accepted Manuscript, which has been through the Royal Society of Chemistry peer review process and has been accepted for publication.

Accepted Manuscripts are published online shortly after acceptance, before technical editing, formatting and proof reading. Using this free service, authors can make their results available to the community, in citable form, before we publish the edited article. We will replace this Accepted Manuscript with the edited and formatted Advance Article as soon as it is available.

You can find more information about Accepted Manuscripts in the [Information for Authors](#).

Please note that technical editing may introduce minor changes to the text and/or graphics, which may alter content. The journal's standard [Terms & Conditions](#) and the [Ethical guidelines](#) still apply. In no event shall the Royal Society of Chemistry be held responsible for any errors or omissions in this Accepted Manuscript or any consequences arising from the use of any information it contains.

## ARTICLE

## Non-Ideal Stoichiometry and Thermochemistry of Aqueous Iridium Oxide Nanoparticles in Proton-Coupled Electron Transfer and Oxygen-Atom Transfer

Justin L. Lee,<sup>§ab</sup> Saeed Saeed,<sup>§a</sup> James M. Mayer\*<sup>a</sup>Received 00th January 20xx,  
Accepted 00th January 20xx

DOI: 10.1039/x0xx00000x

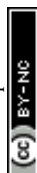
Reported here are reactions of aqueous colloidal IrO<sub>x</sub> nanoparticles (NPs) with proton-coupled electron transfer (PCET) and oxygen-atom transfer (OAT) organic reagents, determining the reaction stoichiometries and thermochemistry. IrO<sub>x</sub> have attracted much attention for their high electrocatalytic activity, but understanding of their fundamental reaction chemistry is limited. This IrO<sub>x</sub> NP model system is simple, with UV-vis titrations demonstrating reversible interconversion between predominantly Ir<sup>IV</sup> and predominantly Ir<sup>III</sup> NPs. This simplicity allows studies that reveal their complex non-idealities. The NP redox chemistry has a “super-Nernstian” stoichiometry of ~1.3 H<sup>+</sup> per 1 e<sup>-</sup> transferred during both PCET and OAT reactions, as measured with electrochemistry and chemical methods. Spectro-electrochemistry revealed a broad distribution of surface IrO<sub>x</sub>-H bond dissociation free energies (BDFE), becoming weaker as more H is added. Such variation in binding strengths—a non-ideal binding isotherm—is common for surface adsorbates. For IrO<sub>x</sub>, the variation of BDFE(IrO-H)s is fit well to a Frumkin isotherm with a width of 6.5 kcal mol<sup>-1</sup>. For OAT from the reactive oxygen atoms of IrO<sub>x</sub> NPs, bracketing experiments gave 93 ± 24 kcal mol<sup>-1</sup> for the average BDFE(O<sub>x</sub>Ir-O), with a predicted spread much larger than that for the BDFE(IrO-H). Taken together, the results show the importance of non-ideal stoichiometry and thermochemistry for IrO<sub>x</sub> NPs, and they open a path to more complete models to understand catalytic redox reactions at such surfaces.

<sup>a</sup> Department of Chemistry, Yale University, New Haven, Connecticut 06520-8107, United States

<sup>b</sup> Department of Chemistry, College of the Holy Cross, Worcester, MA 01610

<sup>§</sup> These authors contributed equally to this work

Supplementary Information available: [details of any supplementary information available should be included here]. See DOI: 10.1039/x0xx00000x

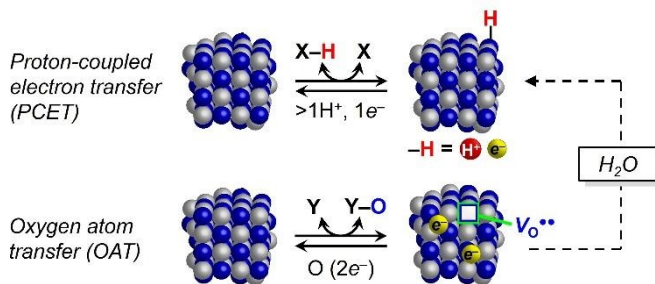


## I. Introduction

Redox reactions at metal-oxide/aqueous interfaces are essential to energy conversion, wastewater treatment, catalysis, corrosion, geochemistry, etc. These processes involve multiple steps on complex surfaces and understanding them at atomistic detail is challenging. While much has been learned from experimental and computational studies of ideal surfaces, most surfaces have defects, irregularities, amorphous regions, and varying M:O:H stoichiometries.<sup>1–5</sup> In addition, electrochemical studies have often implicated >1:1 H<sup>+</sup>/e<sup>-</sup> stoichiometries, termed ‘Super-Nernstian’ behaviour as discussed below.<sup>6–9</sup>

Because of the complexity of oxide/water interfaces, direct experimental measurements of surface reactions are needed. Our approach is to study individual reaction steps on high surface area materials, especially colloidal nanoparticles (NPs).<sup>10–14</sup> While such measurements are an average over the diverse NP surfaces, or perhaps for that reason, some organizing principles are beginning to emerge.

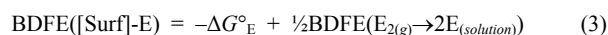
**Scheme 1.** Proton-coupled electron transfer and oxygen atom transfer of metal oxide NPs.



Examined here are redox reactions of aqueous colloidal iridium oxide (IrO<sub>x</sub>) nanoparticles (NPs).<sup>15</sup> IrO<sub>x</sub> materials have long been known to undergo facile proton-coupled electron transfer (PCET) / hydrogen atom transfer (HAT) reactions. We have also recently reported oxygen atom transfer (OAT) reactions from these IrO<sub>x</sub> NPs to molecular substrates.<sup>14</sup> These are some of the most fundamental reaction steps for redox-active oxides, and OAT is a rare example of a multi-electron process at a NP. Scheme 1 shows OAT with an O vacancy (V<sub>O</sub><sup>\*\*</sup>), but lattice and adsorbed oxygen species can be difficult to distinguish for hydrous oxides (see below).<sup>23</sup>

A central parameter for surface reactions is the free energy of adsorption of the various intermediates. According to the Sabatier Principle, a core intuition in heterogeneous catalysis, substrates and products should not bind too strongly or too weakly.<sup>16,17</sup> We have advocated that surface binding energies be quantified similarly to molecular bond strengths, as bond dissociation free energies (BDFEs) (eq 1).<sup>18</sup> Such BDFEs are central to molecular HAT and OAT

reactions.<sup>19–22</sup> The heterogeneous catalysis/surface science literature uses the similar  $\Delta G^\circ_E$  parameter that is defined vs. H<sub>2</sub> or O<sub>2</sub> and is in the opposite direction (eqs 2,3, E = H or O).<sup>16,23–25</sup>  $\Delta G^\circ_H$  is often used as the ‘descriptor’ for multistep catalytic reactions, for instance in ‘volcano plots’ for the electrochemical hydrogen evolution reaction (HER).<sup>26–29</sup>



Surface BDFEs and the Sabatier principle are, however, challenging to use for *real* surfaces. Even for flat, single crystal surfaces, surface–E BDFEs vary with surface coverage ( $\theta_E$ ), typically decreasing at higher  $\theta$ .<sup>1,2,24,30–32</sup> Complex surfaces have various types of surface sites, with different BDFEs. Surfaces thus typically deviate from ‘ideal’ behaviour, with adsorption not well described by the ideal Langmuir isotherm.<sup>5</sup> Understanding non-idealities is particularly important for IrO<sub>x</sub> and related oxides<sup>33,34</sup> because their amorphous, hydrous, or semicrystalline forms can have higher OER activity than single-crystal surfaces.<sup>35–37</sup>

This study uses chemical and electrochemical methods to determine the stoichiometries and thermochemistry of redox reactions of IrO<sub>x</sub> NPs. Studies were limited to Ir<sup>III</sup>–Ir<sup>IV</sup> interconversions to enable reversibility (avoiding catalysis). This report starts with various aspects of PCET reactions, then moves to OAT, and discusses possible links between these reactions.

## II. Results

### II.A. Synthesis & characterization of the IrO<sub>x</sub> NPs

The IrO<sub>x</sub> NPs used in this study were prepared following a procedure from Mallouk *et al.*,<sup>38</sup> by first solvolysis of K<sub>2</sub>IrCl<sub>6</sub> in basic water, then nitric acid-facilitated hydrolysis (SI Section S2, Figure S1). The resulting dark purple colloidal solutions were 1.68±0.01 mM [Ir] (by ICP-MS, see SI Section S2 and Figure S3) and were used without further purification. Characterization of these NPs was reported in our recent OAT study.<sup>14</sup> The studies here were performed at pH 1.86 unless otherwise specified (pH adjusted with aqueous HNO<sub>3</sub> or NaOH, or by dilution with 18 MΩ H<sub>2</sub>O). The IrO<sub>x</sub> NPs were diluted 2-fold with 18 MΩ H<sub>2</sub>O in UV-vis spectroscopic and pH titration experiments ([Ir] = 0.84±0.01 mM), while other experiments used the as-prepared colloids. The optical feature at  $\lambda_{\text{max}} = 568$  nm (top trace in Figure 1A) is a useful spectroscopic handle for quantitative studies.

TEM images showed the NPs to be approximately spherical in shape, with an average diameter of 1.7±0.2 nm (Figures S1, S2A). This corresponds to ~73 Ir atoms per average NP, most of which are estimated to be on the surface (~63 Ir, ~86%, SI Section S2). The large surface-to-core atom ratio is valuable for reactivity and catalytic studies. For simplicity, the as-prepared NPs are called IrO<sub>x</sub> here, even



though they likely had hydrous surfaces and an  $\text{IrO}_x\text{H}_y$  composition.

## II.B. PCET reactivity for $\text{Ir}^{4+/3+}\text{O}_x(\text{H}^+)_m$ NPs

$\text{IrO}_2$  is known to access higher oxidation state, catalytically-active surface species by PCET.<sup>39–43</sup> Murray and Mallouk<sup>30,38</sup> have shown the PCET behaviour of aqueous  $\text{IrO}_x$  NPs by cyclic voltammetry (CV) and rotated disk voltammetry. This section describes thermal PCET reactions of  $\text{IrO}_x$  NPs, their redox stoichiometry and reversibility, CVs as a function of pH, and finally the  $e^-$ -to- $\text{H}^+$  stoichiometry.

### II.B.1. Reduction of as-prepared $\text{IrO}_x$

Addition of 1,4-hydroquinone ( $\text{H}_2\text{Q}$ ) to the aqueous  $\text{IrO}_x$  NPs caused an almost instantaneous bleach of the purple colour. Using small aliquots of  $\text{H}_2\text{Q}$  and monitoring spectrophotometrically, the  $\text{IrO}_x$   $\lambda_{\text{max}} = 568$  nm feature decreased incrementally until an almost-featureless spectrum was reached (black to blue traces in Figure 1). The absorbance plotted in Figure 1B ( $A_{568}$ ) was corrected for the increasing volume of the solution during titrations, and the optical baseline was adjusted to remove the small light scattering of the fully reduced NPs. The titration endpoint showed that  $0.70 \pm 0.01$   $\mu\text{mol}$   $\text{H}_2\text{Q}$  were required (from triplicate measurements). The linearity of the decrease in  $A_{568}$  showed that the  $\text{IrO}_x$  NPs obeyed the Beer-Lambert Law, with  $\epsilon_{568\text{nm}} = 1200 \pm 40 \text{ M}^{-1} \text{ cm}^{-1}$  based on the  $[\text{Ir}] = 0.84 \text{ mM}$ .

A similar titration monitored by  $^1\text{H}$  NMR spectroscopy showed the same endpoint. With increasing  $\text{H}_2\text{Q}$  added, NMR spectra showed its conversion to 1,4-benzoquinone (Q; Figure S5). The  $[\text{Q}]$  increased linearly until the endpoint, and  $\text{H}_2\text{Q}$  was only observed past the endpoint, when there was no further formation of Q. Just as in the UV-vis experiment, the initial dark purple colour was bleached at the NMR endpoint (by eye).

$\text{H}_2\text{Q}$  is a  $2e^-/2\text{H}^+$  PCET reagent, equally well described as a donor of two hydrogen atoms. The  $0.70 \pm 0.01$   $\mu\text{mol}$   $\text{H}_2\text{Q}$  endpoint thus has  $1.40$   $\mu\text{mol}$  of reducing equivalents. The UV-vis titrations started with  $1.68$   $\mu\text{mol}$  of Ir (2 mL of the 2-fold diluted  $1.68 \pm 0.01$  mM as-prepared colloids), so the titration endpoint corresponds to 0.8 reducing equivalents per iridium. This  $\sim 80\%$  reactivity is consistently observed with various PCET, ET, and OAT reagents (*vide infra*).

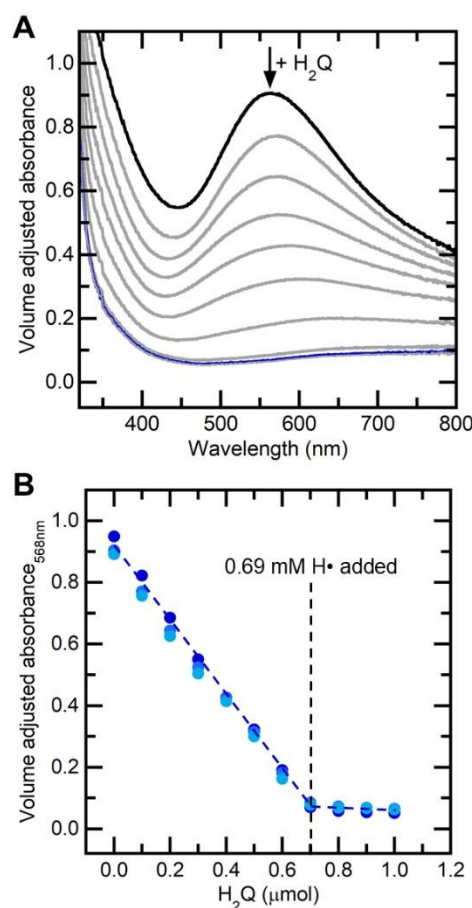


**Figure 1.** A) Spectra from a UV-vis titration of  $\text{IrO}_x + \text{H}_2\text{Q}$ . B) Beer's Law plot of corrected  $A_{568}$  vs.  $\mu\text{mol}$  of  $\text{H}_2\text{Q}$  added.

Based on these observations and the NP oxidation reactions described below, we assign the Ir oxidation state of the as-prepared NPs to be  $\text{Ir}(3.8+)$ .  $\text{IrO}_x$  materials are often found in such non-integer average oxidation states, likely with a delocalized electronic structure as  $\text{IrO}_2$  is metallic.<sup>44</sup> The colourless reduced form at the end of the titration is assigned as essentially all  $\text{Ir}^{\text{III}}$ , as anticipated from the coordination chemistry of iridium and lack of low-energy LMCT or MLCT transitions.<sup>45,46</sup> The 568 nm absorbance has been suggested to be due to an Ir/Ir intervalence charge transfer, for instance on the basis of TD-DFT calculations.<sup>47,48,49</sup> The slight red-shift of the spectrum as the NPs are reduced is perhaps due to the shifts of their reduction potentials and/or to their slight growth, as suggested by the TEM images discussed below.

TEM images after reduction by  $\text{H}_2\text{Q}$  showed  $\text{IrO}_x$  NPs with a diameter of  $1.8 \pm 0.2$  nm (Figure S2B). This is within error of the as-prepared NPs, perhaps with a slight expansion. A slight elongation of the Ir–O bonds would be expected upon reduction due to the increase in the ionic radius. For instance, a  $0.05$  Å increase in the Ir–O bond length was reported for an electrodeposited  $\text{IrO}_2$  film upon reduction.<sup>50</sup>



## ARTICLE

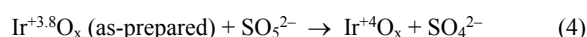
Analogous spectrophotometric redox titrations of the IrO<sub>x</sub> NPs with ascorbic acid and sodium ascorbate (AscH<sub>2</sub> and AscH<sup>-</sup>), with the same spectral changes as in Figure 1A. The same spectra were also obtained in titrations with [Co<sup>II</sup>(bpy)<sub>3</sub>]<sup>2+</sup>, generally considered to be a mild, 1e<sup>-</sup>, outer-sphere reductant (Figure S7).<sup>51</sup>

The endpoints of the AscH<sub>2</sub> and Asc<sup>-</sup> titrations were the same as those with H<sub>2</sub>Q (Figures S8 and S9), as expected because these are all overall 2e<sup>-</sup> reductants. With the Co<sup>II</sup> solution, the endpoint was at twice the number of moles of reagent, within our experimental uncertainty. This is consistent with the reported 1e<sup>-</sup> nature of this reductant.<sup>51</sup> The redox titrations with these reagents thus agree and well define the *redox changes* of the IrO<sub>x</sub> NPs, the number of *electrons* being added or removed. Discussion of the *proton stoichiometries* of these reactions, specifically how many H<sup>+</sup> are taken up by the IrO<sub>x</sub> NPs upon reduction, is deferred to Sections II.B.3 below.

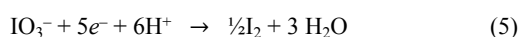
### II.B.2. Reversible redox reactivity of IrO<sub>x</sub> NPs

Oxidation of IrO<sub>x</sub> NPs was accomplished with sodium iodate (NaIO<sub>3</sub>) and with oxone (containing peroxymonosulfate, KHSO<sub>5</sub>). Other OAT reactions of the IrO<sub>x</sub> NPs are described in Section II.D.2 below. We tried but were unable to find an appropriate strong outer-sphere or PCET oxidant, that was stable in these acid solutions and would not chemically change the IrO<sub>x</sub> NPs (*e.g.*, Ce<sup>4+</sup> could bind to the surface).

Oxone oxidized the as-prepared IrO<sub>x</sub> NPs as indicated by a darkening of the purple suspensions. Titration of the as-prepared NPs with Na<sub>2</sub>SO<sub>4</sub> caused little change in the optical spectra (Figure S11), implicating KHSO<sub>5</sub> as the reactive material. Scheme 2 shows images of the suspensions at different iridium oxidation levels. While quantitative titrations were not possible due to the instability of the particles with excess oxone (Figure S12), the results are consistent with eq 4 (which does not indicate the O and H stoichiometries).



Sodium iodate readily oxidized the colourless H<sub>2</sub>Q-reduced IrO<sub>x</sub> NPs but appeared unreactive with the as-prepared NPs. Consistent with this limited reactivity, IO<sub>3</sub><sup>-</sup> oxidized the H<sub>2</sub>Q-reduced IrO<sub>x</sub> NPs only to an absorbance close to that of as-prepared NPs. Iodate is primarily in its IO<sub>3</sub><sup>-</sup> form at pH 1.86, based on its pK<sub>a</sub> of 0.8.<sup>52</sup> Chemically-reduced NPs (generated by treatment with 0.60 μmol H<sub>2</sub>Q [1.2 μmol reducing equivalents]) were re-oxidized by 0.24 μmol IO<sub>3</sub><sup>-</sup>, consistent with the 5 e<sup>-</sup> redox chemistry in eq 5 (see below). The reduction of periodate stops at I<sub>2</sub> because the Ir<sup>3.8</sup>O<sub>x</sub> NPs are not strong enough reductants to form I<sup>-</sup> or I<sub>3</sub><sup>-</sup>. This was confirmed by the *oxidation* of I<sup>-</sup> by as-prepared NPs (see below).



### Scheme 2. Redox Chemistry of IrO<sub>x</sub> NPs

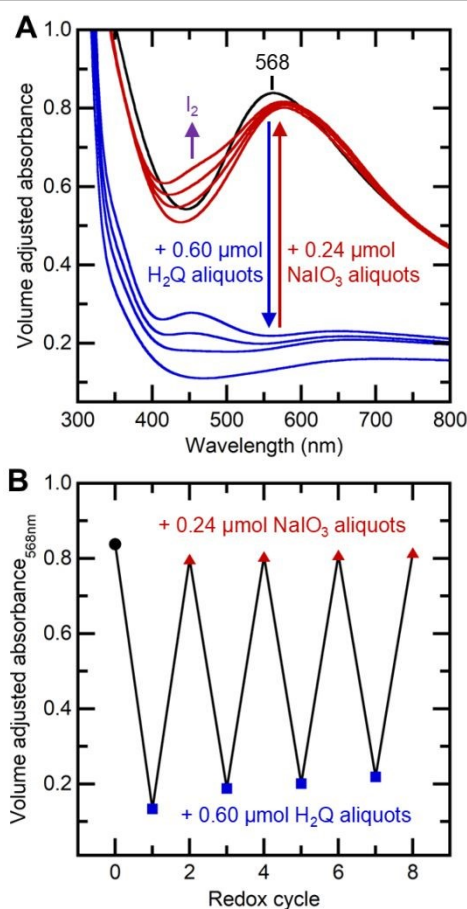
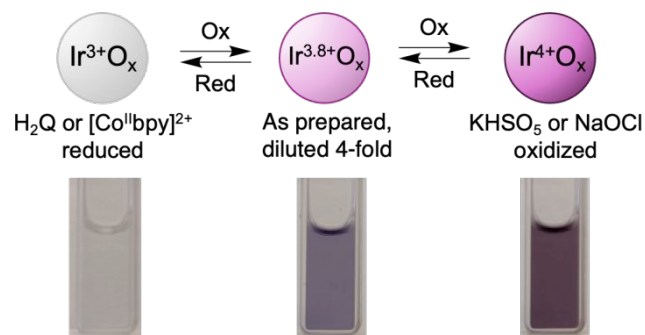


**Figure 2.** Redox cycling of IrO<sub>x</sub> NPs with H<sub>2</sub>Q as the reductant and NaIO<sub>3</sub> as the oxidant. **A)** UV-vis spectra after cycles of reduction (blue arrow and spectra) and oxidation (red arrow and spectra). **B)** Volume-adjusted absorbances after successive cycles of reduction (blue) then oxidation (red).

The IrO<sub>x</sub> NPs can undergo multiple reduction-oxidation cycles with H<sub>2</sub>Q and IO<sub>3</sub><sup>-</sup> (Figure 2). This is consistent with the reversibility of the Ir<sup>4+/3+</sup> couple electrochemically (see <sup>30,38</sup> and the next section). After a few cycles, a distinct feature at λ<sub>max</sub> = 454 nm appeared that is characteristic of I<sub>2</sub>,<sup>53,54</sup> consistent with eq. 5. The optical titrations and the cycling in Figure 2A also show a slightly shifted λ<sub>max</sub> for the IO<sub>3</sub><sup>-</sup>-oxidized



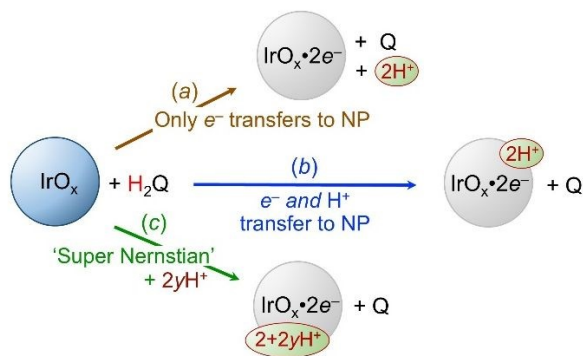
NPs, from the original 568 nm to 575 nm. The magnitude of the absorbance remained relatively constant over the four cycles shown in Figure 2B, while the bleach upon addition of H<sub>2</sub>Q was less complete in later cycles. These changes could be due to the underlying I<sub>2</sub> absorbance and/or to small changes in the NPs upon repeated redox cycling.

### II.B.3. The H<sup>+</sup>/e<sup>-</sup> ratio for PCET reactions of IrO<sub>x</sub> NPs

The pH dependence of the electrochemical properties of IrO<sub>x</sub> NPs and thin films has been examined in several prior studies. Some forms show shifts of 59 mV per pH unit, termed Nernstian behaviour and interpreted as a 1:1 proton-to-electron stoichiometry.<sup>55</sup> However, hydrous forms of IrO<sub>x</sub> (and many other redox-active oxides<sup>6,56</sup> typically have >59 mV/pH slopes (see next Section).<sup>30,57–59</sup> Such super-Nernstian slopes have typically been interpreted as >1:1 H<sup>+</sup>/e<sup>-</sup> ratios, but not always.<sup>60,61</sup> To directly measure the stoichiometry for the NPs examined here, we applied our pH-monitoring approach previously developed for colloidal Au and TiO<sub>2</sub> NPs.<sup>11,13</sup>

>1:1 H<sup>+</sup>/e<sup>-</sup> stoichiometry of our IrO<sub>x</sub> NP redox reactions were measured by chemical titrations with concurrent pH measurements, using [H<sup>+</sup>] = 10<sup>-pH</sup>. If titrations with H<sub>2</sub>Q added only electrons to the IrO<sub>x</sub> NPs, one H<sup>+</sup> would be released from H<sub>2</sub>Q per e<sup>-</sup> (Scheme 3(a), brown top reaction). Alternatively, if H<sub>2</sub>Q transferred H<sup>+</sup> (e<sup>-</sup> + H<sup>+</sup>) to IrO<sub>x</sub>, there would be no change in the [H<sup>+</sup>] (blue reaction, (b)). ‘Super-Nernstian’ behaviour, uptake of greater than 1H<sup>+</sup> per e<sup>-</sup>, would be indicated by a decrease in [H<sup>+</sup>] (green reaction, (c)).

### Scheme 3. Possible H<sup>+</sup> stoichiometries for IrO<sub>x</sub> + H<sub>2</sub>Q



For these experiments, the colloid was initially adjusted with NaOH<sub>(aq)</sub> to pH 2.90–3.10 ([H<sup>+</sup>]<sub>bulk</sub> = 0.79–1.26 mM), so that changes of ±0.1 μmol in the amount of H<sup>+</sup> in the bulk solution could be detected with sufficient accuracy. An aliquot of H<sub>2</sub>Q was added to this solution; after a few minutes both the pH and UV-vis spectra were measured, and the cycle repeated. The spectra (Figure S6) showed the titration endpoint. The experiment was done with three separate solutions to ensure reproducibility.

Experimentally, addition of H<sub>2</sub>Q to these IrO<sub>x</sub> NPs resulted in an increase in pH, i.e., a decrease in the amount of H<sup>+</sup> in

solution. This is shown by the green squares in Figure 3. After the optical titration endpoint, there was little change in the pH with additional H<sub>2</sub>Q. The data showed that, for each reducing equivalent transferred from H<sub>2</sub>Q the NPs, the IrO<sub>x</sub> took up 1.28 H<sup>+</sup>. In addition to the one H<sup>+</sup> per e<sup>-</sup> from the H<sub>2</sub>Q, IrO<sub>x</sub> absorbed 0.28 additional H<sup>+</sup>, in other words, super-Nernstian behaviour (eq 6).

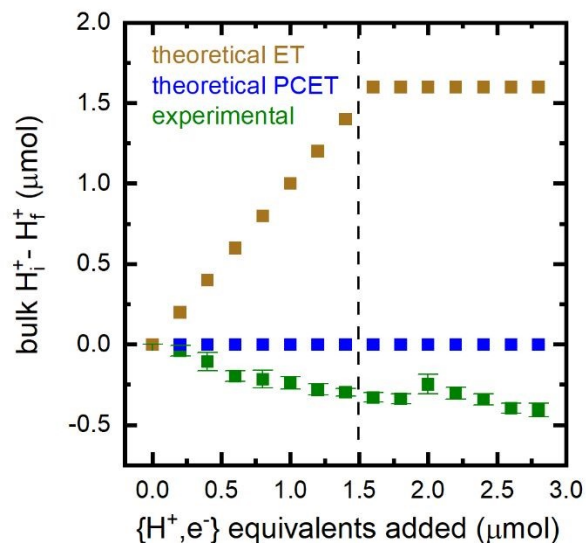


**Figure 3.** Change in bulk H<sup>+</sup> (μmol) upon the addition of H<sup>+</sup>, e<sup>-</sup> (μmol; ½ μmol H<sub>2</sub>Q) calculated from pH change. Brown represents theoretical change for an ET, blue represents change for PCET, green represents experimental results. Experimental data was corrected for dilution effects. Dashed line indicates the optical titration endpoint.



Experiments with the other reductants used above were consistent with the 1.3:1 H<sup>+</sup>:e<sup>-</sup> ratio but the complex speciation of those reagents and their products prevented quantitative analysis of the observed pH changes (see Section S4, Figure S10). The 1.3:1 H<sup>+</sup>:e<sup>-</sup> results agree with the pH electrochemical results from Murray and from our lab (see next section). These results are clearly different from the pure ET and 1:1 e<sup>-</sup>, H<sup>+</sup> PCET pathways in Scheme 3 (see Section III.A below). The ‘extra’ protons in the H<sub>2</sub>Q and other reactions are provided by the pH 1.86 solution, which results from the nitric acid addition in one step of the synthesis.

### II.B.4. Electrochemical properties of IrO<sub>x</sub> NPs

In agreement with prior studies,<sup>30,38,41,42,62</sup> our CVs of these colloidal IrO<sub>x</sub> NPs showed two somewhat indistinct features; we focus here on the lower potential, Ir<sup>IV/III</sup> couple (Figures 4A and S4). The broadness of the waves is typical for CVs of colloidal NPs, and is due to the non-ideal nature of their thermochemistry (described in the next section). The mid-point potential ( $E_{1/2}$ ) of 0.83 V vs. NHE at pH 1.86 is



## ARTICLE

consistent with the result below that as-prepared NPs oxidize I<sup>-</sup> to I<sub>2</sub> or I<sub>3</sub><sup>-</sup> ( $E^\circ = +0.621$  V or  $0.536$  V, respectively).<sup>63</sup>

The  $E_{1/2}$  values from the CVs shifted with pH from 1.5–4, by 78.5 mV per pH unit (Figure 4B). This slope was in excellent agreement with the 75 mV per pH reported by Murray *et al.* for phosphate-buffered IrO<sub>x</sub> NPs in the pH 1–6 range. The close agreement of Murray's and our slopes indicates that this deviation is not a measurement error from the broad waves. These results implicate a PCET process, consistent with the chemical titrations reported above.

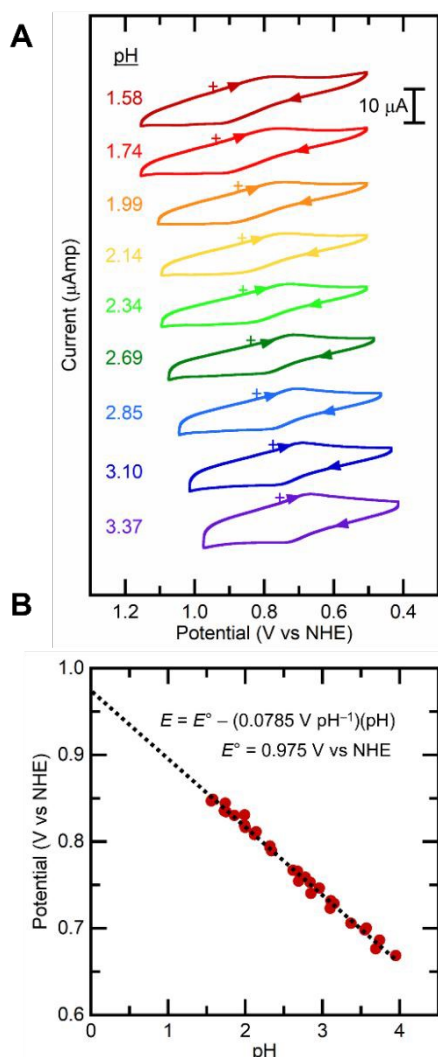
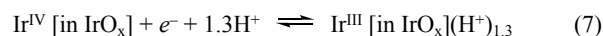


**Figure 4.** A) CVs of aqueous IrO<sub>x</sub> NPs from pH 1.56 – 3.37; the + indicates the open circuit potential. B) Pourbaix plot of  $E_{1/2}$  values vs. pH for the Ir<sup>IV/III</sup> redox couple.

The observed  $E_{1/2}$  vs. pH slopes are ~30 % larger than the 59.2 mV pH<sup>-1</sup> expected for 1:1 H<sup>+</sup>:e<sup>-</sup> transfers at 298 K. Such 'super-Nernstian' slopes, >59.2 mV pH<sup>-1</sup>, are common for hydrous metal oxides and typically interpreted as a >1H<sup>+</sup> per e<sup>-</sup> stoichiometry. From this perspective, the measured slope of 78.5 mV/pH translates into 1.33 H<sup>+</sup>/e<sup>-</sup> (eq 7). This is in

excellent agreement with the proton stoichiometry experiments described in the last section, which gave 1.28 H<sup>+</sup>/e<sup>-</sup>. This agreement is strong confirmation of the proton stoichiometry explanation for the super-Nernstian slope. This result is placed in a broader context in the Discussion below.



## II.C. PCET thermochemistry of [IrO<sub>x</sub>]-H

### II.C.1. Thermochemistry in a super-Nernstian system

A standard 1e<sup>-</sup>/1H<sup>+</sup> PCET reaction is characterized by a free energy  $\Delta G^\circ_{\text{PCET}}$ , a 1e<sup>-</sup> + 1H<sup>+</sup> reduction potential  $E^\circ$ , and an XH BDFE, since 1e<sup>-</sup> + 1H<sup>+</sup>  $\equiv$  H<sup>•</sup> (eq 8). The  $\Delta G^\circ_{\text{PCET}}$  and -BDFE are simply related by the constant  $C_G$ , which is 52.8 kcal mol<sup>-1</sup> in water (eq 9, for  $E^\circ$  vs. NHE at pH 0, or for  $E^\circ$  vs. RHE at any a<sub>H+</sub>).<sup>18</sup>

For 1H<sup>+</sup>/1e<sup>-</sup> reactions:

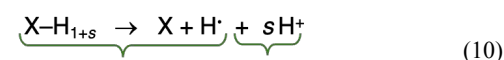


$$\Delta G^\circ_{\text{PCET}} = -FE^\circ(1\text{H}^+/1e^-) = -\text{BDFE}(\text{X-H}) - C_G \quad (9)$$

The IrO<sub>x</sub> NP system, however, transfers 1.3 protons per electron, based on the electrochemical and pH studies in the last two sections. [Such behaviour has been termed super-Nernstian (see reviews<sup>6</sup>) and has been previously reported for hydrous IrO<sub>x</sub> and generally.] The non-1:1 stoichiometry means that the  $\Delta G^\circ$  for reaction 7 is not simply a BDFE. What follows are our initial ideas; we have not found any related thermochemical analyses of super-Nernstian reactions in the literature. We expect to return to this topic in a future publication.

For a super-Nernstian reaction that transfers 1+s protons per electron, the free energy  $\Delta G_{10}$  can be represented as a BDFE plus s times the proton chemical potential  $\mu_{\text{H}^+}$  = -2.303RT × pH (eq 10).

For (1+s)H<sup>+</sup>/1e<sup>-</sup> reactions:



$$\Delta G_{10} = \text{BDFE}(\text{X-H}) + s\mu_{\text{H}^+}$$

For the IrO<sub>x</sub> NP system discussed here, the  $s\mu_{\text{H}^+}$  term is quite small. With  $s = 0.3$  and pH = 1.83,  $s\mu_{\text{H}^+} = 0.8$  kcal mol<sup>-1</sup> (35 meV). Thus, the  $\Delta G_{10}$  and BDFE for IrO<sub>x</sub>-H are numerically close, roughly within the uncertainties of the analysis. To further illustrate that this is a small effect, we return to the E/pH dashed line in Figure 3B above, with a 78.5 mV/pH slope and a y intercept ( $E^\circ$ ) of 0.975 V vs. NHE. Requiring a fixed 1:1 PCET slope of 0.059 V/pH moves the intercept only 1.7 kcal mol<sup>-1</sup> (74 meV) lower at most (Figure S14). We also emphasize that all the thermochemical studies in this report were done at pH 1.86, so that the  $s\mu_{\text{H}^+}$  term is constant and does not affect relative energies. Based on this analysis, *the thermodynamic discussion that follows will ignore the 1.33 H<sup>+</sup>/e<sup>-</sup> stoichiometry and use the normal BDFE parameter.*



II.C.2. A non-ideal isotherm for H-binding to IrO<sub>x</sub> NPs

The measured aqueous PCET  $E_{1/2}$  values extrapolated to pH 0 ( $\cong E^\circ$ ) give the surface BDFE(IrO<sub>x</sub>-H) at standard state. We use 50% coverage ( $\theta_H$ ) as our standard state, where  $\theta_H = 1 - \theta_{Ir^{IV}} = 0.5$ .  $\theta_H = 0$  corresponds to the fully oxidized Ir<sup>IV</sup>O<sub>x</sub>, and  $\theta_H = 1$  indicates the fully reduced Ir<sup>3+</sup> NPs. A system is “ideal” when the values of  $E$  vary with  $\theta_H$  according to the Langmuir isotherm (eq 11). There is a very close analogy between eq 11 and the Nernst equation for a solution potential, where the [Red] relates to  $\theta_H$  and [Ox]  $\equiv 1 - \theta_H$  (eq 17 below). The  $\theta_H = 0.5$  standard state for eq 11 is directly analogous to the [Red] = [Ox] standard state for the Nernst equation.

$$E_{Langmuir} = E^\circ_{\theta=0.5} - 0.059 \log\left(\frac{\theta_H}{1-\theta_H}\right) \quad (11)$$

To experimentally measure the binding isotherm for hydrogen on IrO<sub>x</sub> NPs, we adapted a spectroelectrochemical approach previously developed for nickel oxide electrodes.<sup>32</sup> Briefly, a IrO<sub>x</sub> NP colloid was poised at a specific electrochemical potential by controlled potential electrolysis, and after equilibration the UV-vis spectrum was recorded (Figure 5B). These measurements were conducted at various  $E_{app}$  from 0.53 to 1.13 V vs NHE at pH 1.86; as indicated by dashed and coloured vertical lines in Figure 5A. Applying more anodic potentials resulted in the oxidation beyond Ir<sup>4+</sup>. Further details are discussed in Section S5.

The 568 nm absorbance decreased at more cathodic  $E_{app}$ , where the NPs were more reduced, and increased at anodic  $E_{app}$  (Figure 5B). These changes were fully reversible. Waiting for equilibration and the reversibility of the absorbance show that these experiments measure thermodynamic properties. As established above, the  $A_{568nm}$  directly gives the [Ir<sup>IV</sup>] or,

equivalently, the average oxidation state  $n$  of the Ir (Ir <sup>$n+$</sup> ) (eq 12). This is readily converted to the fraction of the Ir ions that are formally Ir<sup>IV</sup>,  $f(\text{Ir}^{IV})$ , and to the coverage of H (eqs 13,14).

$$A_{568} = \epsilon_{568}[\text{Ir}^{IV}] \quad (12)$$

$$f(\text{Ir}^{IV}) = \frac{A_{568}(E)}{A_{568}(100\% \text{ Ir}^{IV})} \quad (13)$$

$$\theta_H = 1 - f(\text{Ir}^{IV}) = f(\text{Ir}^{III}) \quad (14)$$

The experimental isotherm, the dependence of  $\theta_H$  on  $E_{app}$ , is shown as the coloured points in Figure 5C. The measured isotherm is quite broad, needing a change of 320 mV to move from 10% to 90%  $\theta_H$ . The ideal Langmuir isotherm is much narrower, making this change over only 113 mV (the purple dashed line in Figure 5C). The broadness of the isotherm is the primary origin of the broad CV waves in Figure 4A.

The measurements fit well to a non-ideal *Frumkin isotherm* (black line, eq. 15).<sup>64,65</sup> The century-old Frumkin isotherm simply adds a term linear in  $\theta_H$  to the Langmuir isotherm (eq 11). The conclusion that surface binding is non-ideal is consistent with the discussion above about real surfaces, especially small nanoparticles.<sup>5</sup>

$$E_{Frumkin} = E_{\theta=0.5} - (0.0592 \text{ V}) \log\left(\frac{\theta_H}{1-\theta_H}\right) + C(\theta_H - 0.5) \quad (15)$$

As a check, the midpoint of the fit (0.87 V) is within 40 mV of the  $E_{1/2}$  measured by CV of the colloid at pH 1.86, as it should be. In addition, the isotherm in Figure 5C is consistent with the as-prepared IrO<sub>x</sub> NPs being mostly, but not completely, reduced by excess I<sup>-</sup> (Figure S13). The  $E^\circ(\text{I}_2/\text{I}^-)$  of ~0.62 V lies close to the bottom end of the isotherm, and

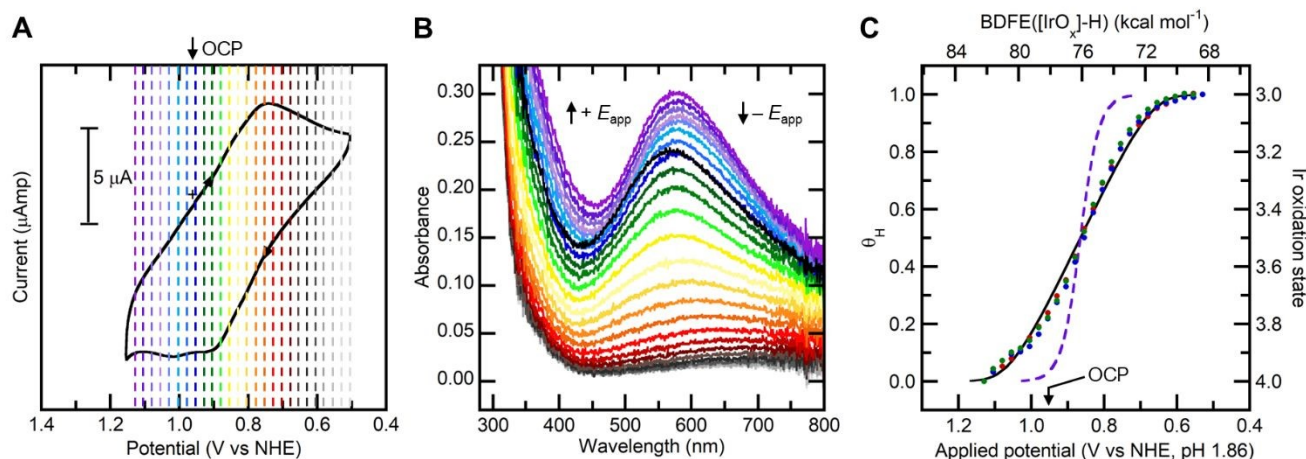


**Figure 5.** A) CV of IrO<sub>x</sub> NPs. Coloured lines indicated applied potential steps at 0.025 V increments. B) Optical spectra at different applied potentials. The colours of the absorbance spectra correspond to the colour of the applied potentials in Figure 5A. C) Plot of hydrogen coverage and Ir oxidation state, as a function of applied potential and BDFE([IrO<sub>x</sub>]-H). Coloured points indicate experimental data fitted to the Frumkin isotherm (black line; eq 15). Purple dashed line corresponds to the H-binding isotherm as described by the Langmuir isotherm (eq 11) and Nernst equation (eq 17 below).



## ARTICLE

the effective potential was higher due to the excess of  $I^-$  over  $I_2$ . The isotherm also predicts  $\theta_H = 0.2$  and  $Ir^{3.8+}$  for the as-prepared NPs, from their open circuit potential (OCP) value (Figure 5C), in agreement with the titrations above. All the results are consistent with this Frumkin isotherm.

Fitting the data to the Frumkin equation gave  $C = 0.28$  V, with free energy  $FC = 0.28$  eV = 6.5 kcal mol<sup>-1</sup>. In some presentations,  $C$  is replaced by the unitless parameter  $g = FC/RT$  (= 11 in this case).<sup>66,67</sup> Given the width of the isotherm, the BDFE([IrO<sub>x</sub>]-H) should be considered to have a range from 73 to 79 kcal mol<sup>-1</sup>, with a midpoint of 76 kcal mol<sup>-1</sup>.

## II.D. OAT reactivity of IrO<sub>x</sub> NPs

We recently reported that IrO<sub>x</sub> NPs can oxidize substrates by oxygen atom transfer, including phosphines to phosphine oxides and a thioether to its sulfoxide (and slowly to the sulfone).<sup>14</sup> Here we extend those studies and compare them with the PCET chemistry described above.

### II.D.1. Comparison of IrO<sub>x</sub> reduction by OAT and PCET reagents

The reduction of IrO<sub>x</sub> NPs by the water-soluble phosphine bis(*p*-sulfonatophenyl)phenylphosphine dianion (PAR<sub>3</sub>) is remarkably similar to the reduction by H<sub>2</sub>Q. The UV-vis titrations of IrO<sub>x</sub> with PAR<sub>3</sub> and H<sub>2</sub>Q showed almost identical spectra and endpoints: 0.66±0.02 μmol for PAR<sub>3</sub> vs. 0.69±0.01 μmol for H<sub>2</sub>Q (Figure S17).<sup>14</sup> This further supports the Ir<sup>3.8+</sup> oxidation state in the as-prepared NPs.

While PAR<sub>3</sub> and H<sub>2</sub>Q are both 2e<sup>-</sup> reductants, phosphines accept O atoms while H<sub>2</sub>Q typically donates H atoms. <sup>18</sup>O studies showed that OAT from IrO<sub>x</sub> to PAR<sub>3</sub> forms some sort of vacant site, which is rapidly filled by a water molecule.<sup>14</sup> The process of O-removal and H<sub>2</sub>O addition apparently forms the same product as the reduction by H<sub>2</sub>Q.<sup>14,68</sup> To confirm this, we repeated the proton stoichiometry titration using PAR<sub>3</sub> instead of H<sub>2</sub>Q. The pH and [H<sup>+</sup>] change with PAR<sub>3</sub> (Figure S18) were essentially identical to those for H<sub>2</sub>Q (Figure 3).

Overall, the similarities between the PAR<sub>3</sub> and H<sub>2</sub>Q reactions reaffirm the implicit assumption above that these reactions are all under thermodynamic control. These are two quite different reagents, but they add the same number of reducing equivalents and form the same IrO<sub>x</sub>H<sub>y</sub> NP product.

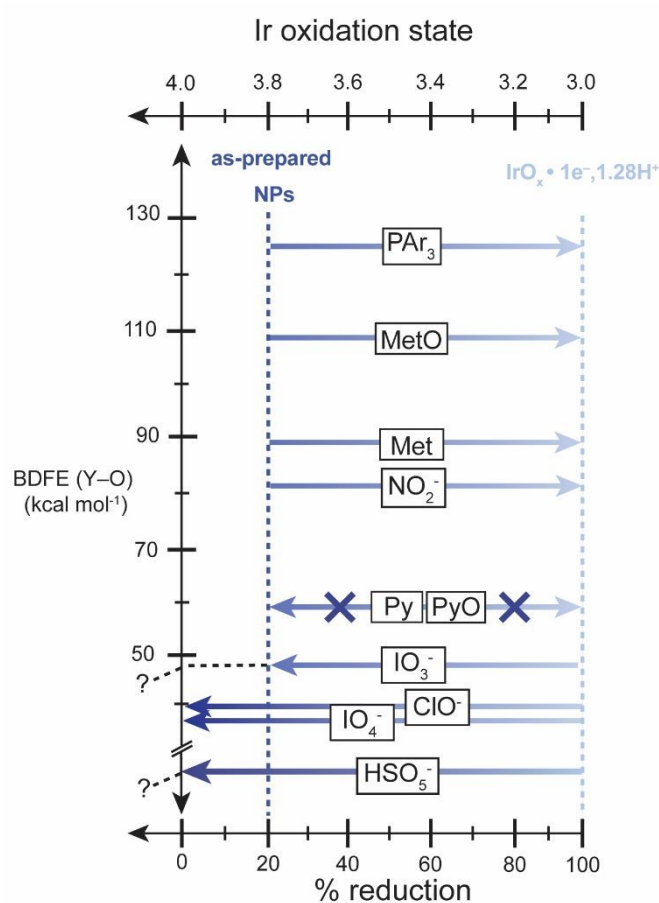
### II.D.2. Thermochemistry and barriers for IrO<sub>x</sub> OAT reactions

The H<sub>2</sub>Q-reduced IrO<sub>x</sub> NPs are oxidized by iodate (IO<sub>3</sub><sup>-</sup>) and oxone (SO<sub>5</sub><sup>2-</sup>),<sup>14</sup> as mentioned above, and also by periodate (IO<sub>4</sub><sup>-</sup>) (Figure S19) and chlorine bleach (NaOCl/Cl<sub>2</sub>) (Figure S20). IO<sub>3</sub><sup>-</sup> oxidizes the NPs roughly to the level of the as prepared material, Ir<sup>3.8+</sup>, but the other reagents take the NPs to the all-Ir<sup>IV</sup> state (Scheme 2 above) and perhaps beyond.

In the other direction, the as-prepared NPs are reduced by PAR<sub>3</sub> and methionine (Figures S21 – S25),<sup>14</sup> and also by excess nitrite (NaNO<sub>2</sub>, Figure S26). Nitrate formation was demonstrated by <sup>15</sup>N NMR (<sup>15</sup>NO<sub>3</sub><sup>-</sup> from <sup>15</sup>NO<sub>2</sub><sup>-</sup>, Figure S27). However, titration with nitrite did not show a sharp endpoint and nitrite is a complicated reagent that can disproportionate in acid solutions.

Many of these net OAT reactions are listed in order of decreasing estimated Y–O BDFEs in Scheme 7 (mostly converted from BDEs: see SI Section S7). As expected, the reagents with high affinities to accept an O atom reduce the IrO<sub>x</sub> NPs (arrows pointing to the right), and those that have weak Y–O bonds are good O-atom donors and oxidize the NPs (arrows to the left).

**Scheme 4.** Summary of IrO<sub>x</sub> net OAT reactions: reagents that reduce the NPs (forward arrows) vs. oxidize the NPs (reverse arrows), listed by estimated BDFE(Y–O).<sup>a</sup>



<sup>a</sup> See SI Section S7 for BDFE references and analysis. No reactions were observed with pyridine or pyridine N-oxide. The horizontal blue



arrows are shaded to mimic the light colour of the reduced NPs (at right) vs. the dark purple of the oxidized NPs (at left). BDFE values for  $\text{IO}_3^-$  and  $\text{HSO}_5^-$  were not found so these arrows are labelled with “?”.

These reagents cover a huge range of driving forces for the OAT reactions, at least 87 kcal mol<sup>-1</sup>. This range of  $\Delta G$  corresponds to a change in  $K_{\text{eq}}$  of  $\geq 10^{64}$ . The results in Scheme 4 provide some insights into the OAT thermochemistry of the  $\text{IrO}_x$  NPs, as discussed below.

In contrast, no reaction was observed between the  $\text{IrO}_x$  NPs and pyridine derivatives. The as-prepared  $\text{IrO}_x$  NPs were not reduced by pyridine (py) or 4-CN-pyridine, and the  $\text{H}_2\text{Q}$ -reduced NPs were not oxidized by pyridine-N-oxide (pyO, Figures S29–S31). The lack of reaction with both py and pyO indicates a kinetic barrier for OAT. In contrast, the HAT/PCET reactions of these  $\text{IrO}_x$  NPs all seem to follow their thermochemistry without substantial kinetic limitation.

### III. Discussion

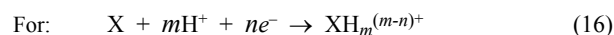
#### III.A. $\text{IrO}_x$ NPs: A simple model system that reveals complexities

From one perspective, this colloidal  $\text{IrO}_x$  NP system is simple. Chemical reactions reversibly cycle the NPs between predominantly  $\text{Ir}^{\text{IV}}$  and predominantly  $\text{Ir}^{\text{III}}$  (for the 80% of the Ir that is redox active). The reaction stoichiometry sets the redox level of the product NPs, so the same thermodynamic product is formed regardless of the reagent. The same product is formed in PCET, HAT, and OAT reactions that give the same average  $\text{Ir}^{m+}$ . This reversibility and generality have enabled understanding of the intrinsic underlying complexity of the  $\text{IrO}_x$  NPs.

Based on our titrations and measurements of total Ir by ICP-MS, 80% of the Ir in these NPs are redox active. Gambarella, Murray, *et al.* reported the same result for  $\text{IrO}_x$  NPs at pH 1.4, using *coulometry (though almost all the Ir were electroactive at higher pHs)*.<sup>30</sup> We previously estimated that the ~1.7 nm  $\text{IrO}_x$  NP diameter corresponds to 4–5 unit cells across and roughly 86% of the Ir are on the surface.<sup>14</sup> While there are uncertainties in both the percent electroactive and the percent at the surface, the values are consistent with the redox reactions and H addition primarily involving surface sites. This is consistent with the lack of a change in size by TEM.<sup>14</sup> However, oxides in water often have a hydrous, partly amorphous shell, which muddies the definition of a surface atom.

All the chemical reactions studied here, PCET, HAT, and OAT, have the same 1.3:1 proton-to-electron stoichiometry, or  $\text{H}^+$  per redox equivalent. The  $\text{H}^+:\text{e}^-$  ratio is important because it determines how the reduction potential varies with pH. This follows from the Nernst or Langmuir equations, with  $[\text{XH}_m^{(m-n)+}]/[\text{X}] \equiv (\theta/(1-\theta))$  (eqs 16–21). Examples with *integer*  $\text{H}^+:\text{e}^-$  ratios are widely recognized, in Pourbaix’s comprehensive Atlas and elsewhere.<sup>69,70</sup>  $E/\text{pH}$  slopes that are not integer multiples of 59 mV/pH ( $m/n$ ) have also long been known and are typically interpreted as a non-integer  $\text{H}^+:\text{e}^-$  stoichiometry. However, other effects could lead to such super-Nernstian slopes. For example, recent papers by Suntivich and co-workers assumed 1:1  $\text{H}^+:\text{e}^-$  ratios and attributed super-Nernstian slopes

to changes in  $E^\circ$ .<sup>7,71,34</sup> For our  $\text{IrO}_x$  NPs, the non-integer stoichiometry was established by a *direct-chemical method*, the change in pH upon reaction (Figure 3), in addition to electrochemistry. The 1.3:1 ratio must be the thermodynamic preference of the  $\text{IrO}_x$ , although the origin of this preference is not known. For these NPs, we take full H coverage,  $\theta_{\text{H}} = 1$ , to be 1.3  $\text{H}^+$  for every  $\text{Ir}^{\text{III}}$ .



$$E_{\text{Nernst}} = E^\circ - \frac{RT}{nF} \ln \left\{ \frac{[\text{XH}_m^{(m-n)+}]}{[\text{X}][\text{H}^+]^m} \right\} \quad (17)$$

$$E_{\text{Langmuir}} = E^\circ_{\theta=0.5} - 0.059 \log \left( \frac{\theta_{\text{H}}}{(1-\theta_{\text{H}})[\text{H}^+]^{m/n}} \right) \quad (18)$$

$$= E^\circ_{\theta=0.5} - (0.0592 \text{ mV}) \left\{ \frac{m}{n} \text{pH} - \log \left( \frac{\theta_{\text{H}}}{(1-\theta_{\text{H}})} \right) \right\} \quad (19)$$

The  $\text{IrO}_x$  NPs studied here have non-ideal H adsorption in terms of both stoichiometry *and* thermochemistry, the adsorption energies following a Frumkin rather than Langmuir isotherm.  $\theta_{\text{H}}$  as a function of pH and  $E_{\text{applied}}$  does *not* follow eqs 18/19. We have not found literature that addresses this case of both non-integer stoichiometry and a non-ideal binding isotherm, and we are not prepared to do this fully here. Still, the model system studies reported here show large non-idealities that are not captured by current models.

To simplify the thermochemical discussions that follow, the remainder of this Discussion will assume a 1:1  $\text{H}^+:\text{e}^-$  stoichiometry. As explained above, this assumption has little numerical effect on the parameters because the pH was kept constant at 1.83 that is close to the standard state of pH 0.

#### III.B. H-atom Binding Energies

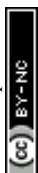
##### III.B.1 Fitting to a Frumkin isotherm

The large surface area, high concentration, and optical absorbance of the  $\text{IrO}_x$  NPs enable the determination of the H-binding isotherm by spectroelectrochemistry (Section II.C). It was established that the system reached equilibrium at each point (each applied potential or amount of reagent).

The measured Frumkin isotherm is about 3 times broader than ideal Langmuir behaviour, with a long linear middle portion. The ratio of  $\text{Ir}^{\text{III}}$  to  $\text{Ir}^{\text{IV}}$  in the NPs changes much more slowly with potential than ideal behaviour. The non-ideality of these  $\text{IrO}_x$  NPs contradicts the common assumption that surface concentrations are good proxies for surface *activities*, and the common assumption of a single free energy of adsorption. The measured isotherm implies a range of  $\text{IrO}_x\text{-H}$  BDFEs, from 73–79 kcal mol<sup>-1</sup>.

The non-ideality of the binding energies is not surprising, as discussed in the next section.<sup>5</sup> To quote and expand Gileadi’s colourful analogy:<sup>67</sup>

“Solid surfaces are rarely homogeneous. There are active sites on which the standard free energy of adsorption is high, and there are less-active sites.... This is much like people entering a movie theater with unmarked seats: the best seats are taken first, and the worst remain for late-comers.”<sup>67</sup> Some like to sit together while others prefer to leave empty seats.



### III.B.2 Generality of the Frumkin isotherm

Frumkin isotherms have been used to describe electrochemical and chemical surface binding for a century.<sup>72</sup> Hydrogen adsorption on metal surfaces has long been known to become weaker with increasingly coverage.<sup>73</sup> The non-ideality is of roughly the same magnitude for H<sub>2</sub> gas adding to metals, and for electrosorption of H<sup>+</sup> onto a Pt(111) crystal face.<sup>74</sup> Frumkin *C* parameters of 0.2-0.3 V have been measured for the first oxidations of hydrous, partially disordered IrO<sub>2</sub> and Co/phosphate films,<sup>33,75</sup> for highly ordered RuO<sub>2</sub>(110) films,<sup>71</sup> for calcined NiO films in contact with various buffers and solvents,<sup>24</sup> and for oleylamine-capped WO<sub>3</sub> nanorods in THF,<sup>31,32,76</sup> in addition to the aqueous colloidal IrO<sub>x</sub> NPs studied here. Yet colloidal, oleate-capped CeO<sub>2-x</sub> NPs in THF have a much broader isotherm,<sup>26</sup> and the 2nd oxidation of the RuO<sub>2</sub>(110) films was almost ideal (*C* close to 0).<sup>71</sup> Theory has provided insights into the differences between the two RuO<sub>2</sub>(110) redox couples (assuming 1:1 H<sup>+</sup>:e<sup>-</sup>).<sup>34</sup>

The generality of the Frumkin isotherm is perhaps surprising. It seems to apply equally well to the highly ordered RuO<sub>2</sub> (110) films, to hydrous, partly amorphous IrO<sub>2</sub> and Co/phosphate films, and the IrO<sub>x</sub> NPs studied here. The 1.7 nm IrO<sub>x</sub> NPs are only a few unit cells across, and a high fraction of surface sites are edges, corners, and defects, if they are faceted at all. Not-so-different results have been obtained with oxides, various single crystal metal surfaces,<sup>73</sup> and metal nanoparticles.<sup>24</sup> The Frumkin isotherm was developed based on inter-adsorbate interactions, but these observations suggest a generality that transcends any single cause.

The Frumkin isotherm is the first-order approximation to a Langmuir isotherm,<sup>67</sup> and can be thought of as the first term of a Taylor series expansion in  $\theta$ . Taking  $a_0$  in eq 20 as the Langmuir isotherm (eq 18), and  $x$  as a small perturbation from that function, the Frumkin linear  $C\theta$  term is simply the  $a_1x$  term. From this perspective, *any small effect that causes deviation from ideality should to a first approximation yield a Frumkin isotherm. The observation of a Frumkin isotherm does not provide insight into the origin of the non-ideality.*

$$f(x) = a_0 + a_1x + a_2x^2 + a_3x^3 + \dots \quad (20)$$

The breadth of the isotherm is likely due to a variety of factors. These including (some of these overlap): *i*) a diversity of surface sites, especially due to the small size of the NPs, *ii*) the range of NP sizes, *iii*) other surface heterogeneities, for instance due to surface O/OH/OH<sub>2</sub> groups, *iv*) inter-adsorbate repulsion (as in Frumkin's original derivation), *v*) changes in the structure and bonding of the nanoparticles upon H addition, *vi*) variability in the points of zero charge, both among different NPs and upon H addition, and *vii*) the presence of surface dipoles. The very broad isotherm for H on CeO<sub>2</sub> nanoparticles was suggested to be due to increasing lattice strain as individual Ce<sup>4+</sup> ions are reduced to localized and form much larger Ce<sup>3+</sup> ions,<sup>26</sup> but this is not the case for IrO<sub>x</sub> due to its metallic bonding and delocalized electrons.

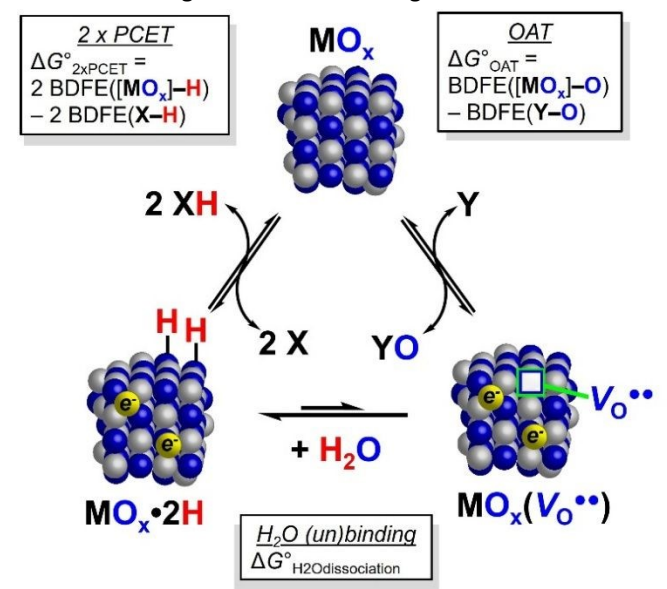
Still, it is remarkable that the isotherm data follow a single, smooth curve. On an irregular surface such as a small NP, one might have expected a subset of the sites to have much higher

or lower affinities for H, which would have led to a more irregular experimental isotherm. Instead, for most materials the Frumkin  $C(\theta - 0.5)$  seems to well describe an average over all the potential non-idealities.

### III.C. Connecting H- and O-atom thermochemistry

OAT and HAT/PCET are two quite different classes of reactions yet the products are related simply by a water molecule, as illustrated in Scheme 5.<sup>68</sup> This stoichiometric connection has long been recognized but is often not highlighted in discussions.<sup>68</sup> Both double H-atom addition and removal of an O-atom result in a 2e<sup>-</sup> reduction. OAT formally gives a vacancy in the NP (V<sub>o</sub>••), which in aqueous media is rapidly filled by H<sub>2</sub>O. This forms the same MO<sub>x</sub>•2H as HAT/PCET to the NP. This equivalence is evident for the IrO<sub>x</sub> reactions with H<sub>2</sub>Q and PAR<sub>3</sub> discussed above, in their identical titration endpoints and amounts of proton uptake.

**Scheme 5.** Triangle scheme connecting HAT and OAT



The triangle scheme in Scheme 5 also serves as a thermochemical cycle between PCET and OAT reactivity. Because it is a closed loop, the sum of the three  $\Delta G^\circ$ s around the cycle must be zero, as shown in eq 21 moving counter-clockwise from the oxidized form at top. This equation allows the calculation of any free energy from the other two. While more work is needed to experimentally define the  $\Delta G^\circ$ (OAT to Y) and  $\Delta G^\circ$ (H<sub>2</sub>O binding to V<sub>o</sub>••), this connection between HAT and OAT provides valuable insights.

$$\Delta G^\circ(\text{OAT to Y}) + \Delta G^\circ(\text{H}_2\text{O binding to } V_o^{\bullet\bullet}) + 2\Delta G^\circ(\text{HAT to X}) = 0 \quad (21)$$

The  $\Delta G^\circ$  for H<sub>2</sub>O dissociation (bottom of Scheme 5) is thus a key parameter in connecting HAT and OAT thermochemistry.<sup>59</sup> Unfortunately, we have found little information about H<sub>2</sub>O binding energies in aqueous solutions when the O being lost is formally a lattice oxygen [the product of OAT] (SI Section S7). Calculations of H<sub>2</sub>O binding energies for an ideal, oxidized,



stoichiometric  $(\text{IrO}_2)_{115}(\text{H}_2\text{O})_{88}$  nanoparticle in vacuo gave  $\Delta G^\circ_{\text{H}_2\text{O diss}}$  values from  $-26$  to  $-36$  kcal mol $^{-1}$ .<sup>77</sup> The binding energy for  $\text{H}_2\text{O}$  to a bare  $\text{RuO}_2$  surface was calculated to be  $-33$  kcal mol $^{-1}$ .<sup>78</sup>

Following this kind of analysis, the OAT thermochemistry of the  $\text{IrO}_x$  NPs is bracketed by the ladder of reactions in Scheme 4 above (see SI Section S7). This approach has long been used in molecular and solid-state chemistries. For instance, Soper *et al.* bracketed the BDE of a  $\text{V}^{\text{V}}\equiv\text{O}$  bond in to be  $73\pm 14$  kcal mol $^{-1}$ <sup>79</sup> by reacting its complex with seven OAT reagents with  $60 < \text{BDE}[\text{Y}-\text{O}] < 133$  kcal mol $^{-1}$ .<sup>20,80</sup> The free energies for loss of  $\text{O}_2$  from solid binary metal oxides as a function of temperature were summarized in an 'Ellingham diagram' 80 years ago.<sup>81</sup>

For  $\text{IrO}_x$  NPs, the driving force for the OAT reactions includes both the  $\text{O}_x\text{Ir}-\text{O}$  BDFE and the  $\Delta G^\circ$  for  $\text{H}_2\text{O}$  binding. This  $\text{H}_2\text{O}$  binding is specifically to the oxygen vacancy resulting from  $\text{Ir}-\text{O}$  bond cleavage (Scheme 5). With this approach, the ladder of OAT reactions in Scheme 4 brackets of the combination of the  $\text{BDFE}(\text{O}_x\text{Ir}-\text{O})$  and the  $\Delta G^\circ_{\text{H}_2\text{O binding}}$  (eq 22, in kcal mol $^{-1}$ ). Unfortunately, this analysis gives only a broad range because reagents with intermediate  $\text{Y}-\text{O}$  BDFEs, such as  $\text{pyO}$ , were kinetically unreactive. If  $\Delta G^\circ_{\text{H}_2\text{O binding}}$  is taken to be  $-30$  kcal mol $^{-1}$ ,  $\text{BDFE}(\text{Ir}-\text{O})$  is estimated to be  $93 \pm 24$  kcal mol $^{-1}$  (eq 23)

$$\sim 87 (\text{Met}) > \text{BDFE}(\text{O}_x\text{Ir}-\text{O}) - \Delta G^\circ_{\text{H}_2\text{O binding}} > \sim 40 (\text{IO}_4^-) \quad (22)$$

$$\text{With } \Delta G^\circ_{\text{H}_2\text{O binding}} \sim -30 \text{ kcal mol}^{-1},$$

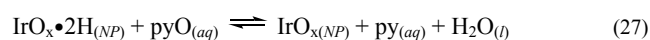
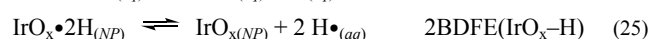
$$117 > \text{BDFE}(\text{O}_x\text{Ir}-\text{O}) > 70, \text{ or} \quad (23)$$

$$\text{BDFE}(\text{O}_x\text{Ir}-\text{O}) = 93 \pm 24 \text{ kcal mol}^{-1}$$

Thermochemical cycles such as Scheme 5 can be used in multiple ways. For instance, Scheme 6 shows how the  $\Delta G^\circ$  for the pyridine  $\text{N}$ -oxide ( $\text{pyO}_{(aq)}$ ) oxidation of fully reduced  $\text{IrO}_x\text{H}_n$  NPs (eq 25) by can be determined without knowledge of the  $\Delta G^\circ_{\text{H}_2\text{O binding}}$ . The  $\text{O}$  removed from  $\text{pyO}$  is transferred to solution (eq 24) and then picks up two  $\text{H}$  from the reduced  $\text{IrO}_x$  NPs (eqs 25 and 26) to form the product water. The  $\Delta G^\circ$  (eq 27) is estimated to be  $-13$  kcal mol $^{-1}$ . More details and references are given in SI Section S7, together with a related calculation for OAT to methionine.

Under the pH 1.83 reaction conditions, the product  $\text{py}$  of reaction 27 will be protonated, which will add more driving force. Yet this reaction does not proceed. The absence of reaction is therefore due to a kinetic barrier ( $\Delta G^\ddagger$ ), and not due to the reaction being uphill. This contrasts with the HAT/PCET reactions above that seem to parallel the thermochemistry in all cases.

**Scheme 6.**  $\Delta G^\circ$  for  $\text{IrO}_x\text{H}_n + \text{pyO} \rightarrow \text{IrO}_x + \text{py} + \text{H}_2\text{O}$



$$\Delta G^\circ_{(25)} = 2\text{BDFE}(\text{IrO}_x-\text{H}) + \text{BDFE}(\text{Y}-\text{O}) - \Delta G^\circ_{\text{H}_2\text{O}(l),\text{atom}}$$

### III.E. Non-Ideality in O-atom thermochemistry

The next layer of the thermochemical analysis of O-atom transfer reactions is the likelihood of broad ranges of the OAT free energy parameters. Scheme 5 and eq 21 show that OAT is related to twice the HAT energetics, so to a first approximation the spread of  $\text{Ir}-\text{O}$  BDFEs should be twice that of the  $\text{IrO}-\text{H}$  BDFEs, or ca.  $\sim 13$  kcal mol $^{-1}$ . This follows from an O-atom being a  $2e^-$  oxidant vs. the  $1e^-$  reductant  $\text{H}\cdot$ .

The range of  $\text{H}_2\text{O}$  binding energies noted above will also contribute to the non-ideality of O-atom binding. The calculations of the ideal  $(\text{IrO}_2)_{115}(\text{H}_2\text{O})_{88}$  NP mentioned above found eleven different Ir binding sites for water, and that hydrogen-bonding networks were important.<sup>77</sup> The diversity of sites, H-bonding networks, and binding energies is likely even larger for our hydrous  $\text{IrO}_x$  NPs in aqueous solution. Perhaps most importantly, we have yet no information about which of the possible water dissociations form a vacancy that can accept an O atom.

A combined surface-science and DFT study examined 4-layer (9Å) films of rutile  $\text{IrO}_2(100)$  grown on an  $\text{Ir}(111)$  crystal surface.<sup>82</sup> The surface was "oxygen-rich" with roughly one O per Ir beyond the stoichiometric  $\text{IrO}_2(100)$  surface, in the less-stable atop binding configuration.  $\text{BDFE}(\text{Ir}-\text{O})$  for these extra O was very small, decreasing from 23-18 kcal mol $^{-1}$  with increasing O coverage. Considering all the surface  $\text{Ir}-\text{O}$  bonds, the calculations showed a 47 kcal mol $^{-1}$  binding energy range.

These calculations show the remarkable diversity and complexity of  $\text{IrO}_2$  single crystal and idealized NP surfaces. For our  $\text{IrO}_x$  NPs, the chemistry of  $\text{Ir}-\text{O}$  bonds will be more complex than that of  $\text{IrO}-\text{H}$  bonds.

## IV. Conclusions

The redox reactions of aqueous colloidal  $\text{IrO}_x$  NPs are non-ideal in both their stoichiometry and thermochemistry.

These 1.7 nm-diameter NPs in acidic water have been developed a simple model system for interfacial reactivity at a redox-active metal oxide. Focusing only on the  $\text{Ir}^{\text{IV}}/\text{Ir}^{\text{III}}$  redox couple, various PCET/HAT ( $e^- + \text{H}^+$ ) and oxygen-atom transfer (OAT) reactions are reversible, with  $\sim 80\%$  of the Ir ions electroactive. The colloids can be set at any average Ir redox level, and the same thermodynamic product is formed with each reagent.

The reactions of the  $\text{IrO}_x$  NPs all have the same 'super-Nernstian' stoichiometry, with 1.3 protons adding to the  $\text{IrO}_x$  surface with each electron added. The non-integer stoichiometry was demonstrated electrochemically and by directly measuring the  $\text{H}^+$  taken up upon reduction. Non-integer PCET is common for hydrous oxides,<sup>30,57-59</sup> but its origin is not well understood.

Spectroelectrochemical studies showed that changes in the  $[\text{Ir}^{\text{IV}}]/[\text{Ir}^{\text{III}}]$  ratio in the NPs required much larger changes in applied potential than predicted by the Nernst equation. The data fit well to a non-ideal Frumkin isotherm. Approximating the reactions as H-atom transfers ( $1\text{H}^+ : 1e^-$ ), the distribution of  $\text{BDFE}([\text{IrO}_x]-\text{H})$  has a midpoint of 76 kcal mol $^{-1}$  and a spread of 6.5 kcal mol $^{-1}$  as a function of H saturation ( $\theta_{\text{H}}$ ). The isotherm for O-atom removal from the  $\text{IrO}_x$  NPs is estimated to be much



wider than that for HAT, due in part to OAT being a formal 2e<sup>-</sup> transfer.

The non-ideal stoichiometry and thermochemistry are core features of the redox chemistry of this ‘simple’ IrO<sub>x</sub> NP model system—and many others. Oxide-water interfaces should not be assumed to follow ideal Nernstian or Langmuirian behaviour (as is often done). The thermochemistry very nicely fits a simple two-parameter Frumkin isotherm, and the reason for the generality of this isotherm is discussed. The accuracy of the mathematically simple Frumkin isotherm provides quantitative understanding and provides a path forward to more realistic models. New models are needed because the non-ideality of (nano)-materials is likely an advantage in many applications.

### Author contributions

The conception of the project was by J.L.L. and J.M.M., and the experiments and analyses were performed by J.L.L. and S.S. J.M.M. was the research advisor, assisting with project goal selection, project focus, and experiment interpretation. All authors participated in manuscript preparation and editing, with final editing by J.M.M.

### Conflicts of interest

There are no conflicts to declare.

### Data availability

The datasets supporting this article have been uploaded as part of the Electronic Supplementary Information.

### Acknowledgements

This research made extensive use of Yale University's Chemical and Biophysical Instrumentation Center (CBIC; RRID:SCR\_021738; equipment was purchased with funds from Yale University). We also thank the Yale Institute for Nanoscience and Quantum Engineering (YINQE) and Dr. Sungwoo Sohn, and the Yale Analytical and Stable Isotope Center (YASIC) and Jonas Karosas. The work was funded predominantly by the U.S. Department of Energy, Office of Science, Basic Energy Sciences (award No. DE-SC0021298).

### Notes and references

- Halsey, G. D. The Role of Surface Heterogeneity in Adsorption. In *Advances in Catalysis*; Elsevier, 1952; Vol. 4, pp 259–269. [https://doi.org/10.1016/S0360-0564\(08\)60616-1](https://doi.org/10.1016/S0360-0564(08)60616-1).
- Boudart, M. Kinetics on Ideal and Real Surfaces. *AIChE Journal* **1956**, *2* (1), 62–64. <https://doi.org/10.1002/aic.690020113>.
- Brown, G. E.; Henrich, V. E.; Casey, W. H.; Clark, D. L.; Eggleston, C.; Felmy, A.; Goodman, D. W.; Grätzel, M.; Maciel, G.; McCarthy, M. I.; Nealsen, K. H.; Sverjensky, D. A.; Toney, M. F.; Zachara, J. M. Metal Oxide Surfaces and Their Interactions with Aqueous Solutions and Microbial Organisms. *Chem. Rev.* **1999**, *99* (1), 77–174. <https://doi.org/10.1021/cr980011z>.
- Carvalho, O. Q.; Adiga, P.; Murthy, S. K.; Fulton, J. L.; Gutiérrez, O. Y.; Stoerzinger, K. A. Understanding the Role of Surface Heterogeneities in Electrosynthesis Reactions. *iScience* **2020**, *23* (12), 101814. <https://doi.org/10.1016/j.isci.2020.101814>.
- Mayer, J. M. Site Heterogeneity and Broad Surface-Binding Isotherms in Modern Catalysis: Building Intuition beyond the Sabatier Principle. *Journal of Catalysis* **2024**, *439*, 115725. <https://doi.org/10.1016/j.jcat.2024.115725>.
- Burke, L. D.; Lyons, M. E. G. Electrochemistry of Hydrated Oxide Films. In *Modern Aspects of Electrochemistry*; White, R. E., Bockris, J. O., Conway, B. E., Eds.; Modern Aspects of Electrochemistry; Springer US: Boston, MA, 1986; Vol. 18, pp 169–248. <https://doi.org/10.1007/978-1-4613-1791-3>.
- Kuo, D.-Y.; Kawasaki, J. K.; Nelson, J. N.; Kloppenburg, J.; Hautier, G.; Shen, K. M.; Schlom, D. G.; Suntivich, J. Influence of Surface Adsorption on the Oxygen Evolution Reaction on IrO<sub>2</sub> (110). *J. Am. Chem. Soc.* **2017**, *139* (9), 3473–3479. <https://doi.org/10.1021/jacs.6b11932>.
- Liang, C.; Katayama, Y.; Tao, Y.; Morinaga, A.; Moss, B.; Celorrio, V.; Ryan, M.; Stephens, I. E. L.; Durrant, J. R.; Rao, R. R. Role of Electrolyte pH on Water Oxidation for Iridium Oxides. *J. Am. Chem. Soc.* **2024**, *146* (13), 8928–8938. <https://doi.org/10.1021/jacs.3c12011>.
- Holzappel, N. P.; Augustyn, V.; Balland, V. Fundamentals of Proton-Insertion Coupled Electron Transfer (PICET) in Metal Oxides for Aqueous Batteries. *ACS Energy Letters* **2025**, *10* (3), 1143–1164. <https://doi.org/10.1021/acscenergylett.4c03076>.
- Valdez, C. N.; Schimpf, A. M.; Gamelin, D. R.; Mayer, J. M. Proton-Controlled Reduction of ZnO Nanocrystals: Effects of Molecular Reductants, Cations, and Thermodynamic Limitations. *J. Am. Chem. Soc.* **2016**, *138* (4), 1377–1385. <https://doi.org/10.1021/jacs.5b12182>.
- Peper, J. L.; Gentry, N. E.; Boudy, B.; Mayer, J. M. Aqueous TiO<sub>2</sub> Nanoparticles React by Proton-Coupled Electron Transfer. *Inorganic Chemistry* **2022**, *61* (2), 767–777. <https://doi.org/10.1021/acs.inorgchem.1c03125>.
- Agarwal, R. G.; Mayer, J. M. Coverage-Dependent Rate-Driving Force Relationships: Hydrogen Transfer from Cerium Oxide Nanoparticle Colloids. *J. Am. Chem. Soc.* **2022**, *144* (45), 20699–20709. <https://doi.org/10.1021/jacs.2c07988>.
- Gentry, N. E.; Kurimoto, A.; Cui, K.; Cleron, J. L.; Xiang, C. M.; Hammes-Schiffer, S.; Mayer, J. M. Hydrogen on Colloidal Gold Nanoparticles. *J. Am. Chem. Soc.* **2024**, *146* (21), 14505–14520. <https://doi.org/10.1021/jacs.4c00507>.
- Lee, J. L.; Gentry, N. E.; Peper, J. L.; Hetzel, S.; Quist, C.; Menges, F. S.; Mayer, J. M. Oxygen Atom Transfer Reactions of Colloidal Metal Oxide Nanoparticles. *ACS Nano* **2025**, *19* (10), 10289–10300. <https://doi.org/10.1021/acsnano.4c17955>.
- Zhao, Y.; Hernandez-Pagan, E. A.; Vargas-Barbosa, N. M.; Dysart, J. L.; Mallouk, T. E. A High Yield Synthesis of Ligand-Free Iridium Oxide Nanoparticles with High Electrocatalytic Activity. *J. Phys. Chem. Lett.* **2011**, *2* (5), 402–406. <https://doi.org/10.1021/jz200051c>.
- Medford, A. J.; Vojvodic, A.; Hummelshøj, J. S.; Voss, J.; Abild-Pedersen, F.; Studt, F.; Bligaard, T.; Nilsson, A.; Nørskov, J. K. From the Sabatier Principle to a Predictive Theory of Transition-Metal Heterogeneous Catalysis. *Journal of Catalysis* **2015**, *328*, 36–42. <https://doi.org/10.1016/j.jcat.2014.12.033>.



- 17 Ooka, H.; Huang, J.; Exner, K. S. The Sabatier Principle in Electrocatalysis: Basics, Limitations, and Extensions. *Front. Energy Res.* **2021**, *9*, 654460. <https://doi.org/10.3389/fenrg.2021.654460>.
- 18 Agarwal, R. G.; Coste, S. C.; Groff, B. D.; Heuer, A. M.; Noh, H.; Parada, G. A.; Wise, C. F.; Nichols, E. M.; Warren, J. J.; Mayer, J. M. Free Energies of Proton-Coupled Electron Transfer Reagents and Their Applications. *Chemical Reviews* **2022**, *122* (1), 1–49. <https://doi.org/10.1021/acs.chemrev.1c00521>.
- 19 Mayo, F. R. Rate Constants in the Gas-Phase Oxidation of Alkanes and Alkyl Radicals. In *Oxidation of organic compounds*; Advances in Chemistry; American Chemical Society, Washington, DC; Vol. 2.
- 20 Holm, R. H. Metal-Centered Oxygen Atom Transfer Reactions. *Chemical Reviews* **1987**, *87* (6), 1401–1449.
- 21 Mayer, J. M. Understanding Hydrogen Atom Transfer: From Bond Strengths to Marcus Theory. *Acc. Chem. Res.* **2011**, *44* (1), 36–46. <https://doi.org/10.1021/ar100093z>.
- 22 Campbell, C. T. Energies of Adsorbed Catalytic Intermediates on Transition Metal Surfaces: Calorimetric Measurements and Benchmarks for Theory. *Acc. Chem. Res.* **2019**, *52* (4), 984–993. <https://doi.org/10.1021/acs.accounts.8b00579>.
- 23 Nørskov, J. K.; Bligaard, T.; Logadottir, A.; Bahn, S.; Hansen, L. B.; Bollinger, M.; Bengaard, H.; Hammer, B.; Slijivancanin, Z.; Mavrikakis, M.; Xu, Y.; Dahl, S.; Jacobsen, C. J. H. Universality in Heterogeneous Catalysis. *Journal of Catalysis* **2002**, *209* (2), 275–278. <https://doi.org/10.1006/jcat.2002.3615>.
- 24 García-Diéguez, M.; Hibbitts, D. D.; Iglesia, E. Hydrogen Chemisorption Isotherms on Platinum Particles at Catalytic Temperatures: Langmuir and Two-Dimensional Gas Models Revisited. *J. Phys. Chem. C* **2019**, *123* (13), 8447–8462. <https://doi.org/10.1021/acs.jpcc.8b10877>.
- 25 Paal, Z.; Menon, P. G. *Hydrogen Effects in Catalysis*; CRC Press, 2020. <https://doi.org/10.1201/9781003065807>.
- 26 Conway, B. E.; Bockris, J. O. Electrolytic Hydrogen Evolution Kinetics and Its Relation to the Electronic and Adsorptive Properties of the Metal. *The Journal of Chemical Physics* **1957**, *26* (3), 532–541. <https://doi.org/10.1063/1.1743339>.
- 27 Bligaard, T.; Nørskov, J. K.; Dahl, S.; Matthiesen, J.; Christensen, C. H.; Sehested, J. The Brønsted–Evans–Polanyi Relation and the Volcano Curve in Heterogeneous Catalysis. *Journal of Catalysis* **2004**, *224* (1), 206–217. <https://doi.org/10.1016/j.jcat.2004.02.034>.
- 28 Zheng, J.; Sheng, W.; Zhuang, Z.; Xu, B.; Yan, Y. Universal Dependence of Hydrogen Oxidation and Evolution Reaction Activity of Platinum-Group Metals on pH and Hydrogen Binding Energy. *Sci. Adv.* **2016**, *2* (3), e1501602. <https://doi.org/10.1126/sciadv.1501602>.
- 29 Dubouis, N.; Grimaud, A. The Hydrogen Evolution Reaction: From Material to Interfacial Descriptors. *Chem. Sci.* **2019**, *10* (40), 9165–9181. <https://doi.org/10.1039/C9SC03831K>.
- 30 Gambardella, A. A.; Borge, N. S.; Alspaugh, V. K.; Murray, R. W. Voltammetry of Diffusing 2 Nm Iridium Oxide Nanoparticles. *Journal of Physical Chemistry C* **2011**, *115* (44), 21659–21665. <https://doi.org/10.1021/jp206987z>.
- 31 Agarwal, R. G.; Kim, H. J.; Mayer, J. M. Nanoparticle O-H Bond Dissociation Free Energies from Equilibrium Measurements of Cerium Oxide Colloids. *Journal of the American Chemical Society* **2021**, *143* (7), 2896–2907. <https://doi.org/10.1021/jacs.0c12799>.
- 32 Noh, H.; Mayer, J. M. Medium-Independent Hydrogen Atom Binding Isotherms of Nickel Oxide Electrodes. *Chem* **2022**, *8* (12), 3324–3345. <https://doi.org/10.1016/j.chempr.2022.08.018>.
- 33 Liang, C.; Rao, R. R.; Svane, K. L.; Hadden, J. H. L.; Moss, B.; Scott, S. B.; Sachs, M.; Murawski, J.; Frandsen, A. M.; Riley, D. J.; Ryan, M. P.; Rossmeisl, J.; Durrant, J. R.; Stephens, I. E. L. Unravelling the Effects of Active Site Density and Energetics on the Water Oxidation Activity of Iridium Oxides. *Nat Catal* **2024**, *7* (7), 763–775. <https://doi.org/10.1038/s41929-024-01168-7>.
- 34 Zhang, L.; Kloppenburg, J.; Lin, C.-Y.; Mitrovic, L.; Gelin, S.; Dabo, I.; Schlom, D. G.; Suntivich, J.; Hautier, G. Atomistic Understanding of Hydrogen Coverage on RuO<sub>2</sub> (110) Surface under Electrochemical Conditions from *Ab Initio* Statistical Thermodynamics. *J. Phys. Chem. C* **2025**, *129* (8), 4043–4051. <https://doi.org/10.1021/acs.jpcc.4c07229>.
- 35 Reier, T.; Teschner, D.; Lunkenbein, T.; Bergmann, A.; Selve, S.; Kraehnert, R.; Schlögl, R.; Strasser, P. Electrocatalytic Oxygen Evolution on Iridium Oxide: Uncovering Catalyst-Substrate Interactions and Active Iridium Oxide Species. *J. Electrochem. Soc.* **2014**, *161* (9), F876–F882. <https://doi.org/10.1149/2.0411409jes>.
- 36 Yu, H.; Liao, F.; Zhu, W.; Qin, K.; Shi, J.; Ma, M.; Li, Y.; Fang, M.; Su, J.; Song, B.; Li, L.; Zairov, R. R.; Ji, Y.; Shao, M.; Shao, Q. Two-Dimensional Amorphous Iridium Oxide for Acidic Oxygen Evolution Reaction. *ChemCatChem* **2023**, *15* (19), e202300737. <https://doi.org/10.1002/cctc.202300737>.
- 37 Mom, R. V.; Falling, L. J.; Kasian, O.; Algara-Siller, G.; Teschner, D.; Crabtree, R. H.; Knop-Gericke, A.; Mayrhofer, K. J. J.; Velasco-Vélez, J.-J.; Jones, T. E. Operando Structure–Activity–Stability Relationship of Iridium Oxides during the Oxygen Evolution Reaction. *ACS Catal.* **2022**, *12* (9), 5174–5184. <https://doi.org/10.1021/acscatal.1c05951>.
- 38 Zhao, Y.; Hernandez-Pagan, E. A.; Vargas-Barbosa, N. M.; Dysart, J. L.; Mallouk, T. E. A High Yield Synthesis of Ligand-Free Iridium Oxide Nanoparticles with High Electrocatalytic Activity. *Journal of Physical Chemistry Letters* **2011**, *2* (5), 402–406. <https://doi.org/10.1021/jz200051c>.
- 39 Gao, J.; Liu, Y.; Liu, B.; Huang, K. W. Progress of Heterogeneous Iridium-Based Water Oxidation Catalysts. *ACS Nano* **2022**, *16* (11), 17761–17777. <https://doi.org/10.1021/acsnano.2c08519>.
- 40 Sharma, R.; Karlsen, M. A.; Morgen, P.; Chamier, J.; Ravnsbæk, D. B.; Andersen, S. M. Crystalline Disorder, Surface Chemistry, and Their Effects on the Oxygen Evolution Reaction (OER) Activity of Mass-Produced Nanostructured Iridium Oxides. *ACS Applied Energy Materials* **2021**, *4* (3), 2552–2562. <https://doi.org/10.1021/acsaem.0c03127>.
- 41 Bozal-Ginesta, C.; Rao, R. R.; Mesa, C. A.; Liu, X.; Hillman, S. A. J.; Stephens, I. E. L.; Durrant, J. R. Redox-State Kinetics in Water-Oxidation IrOx Electrocatalysts Measured by Operando Spectroelectrochemistry. *ACS Catalysis* **2021**, *11* (24), 15013–15025. <https://doi.org/10.1021/acscatal.1c03290>.
- 42 Bozal-Ginesta, C.; Rao, R. R.; Mesa, C. A.; Wang, Y.; Zhao, Y.; Hu, G.; Antón-García, D.; Stephens, I. E. L.; Reisner, E.; Brudvig, G. W.; Wang, D.; Durrant, J. R. Spectroelectrochemistry of Water Oxidation Kinetics in Molecular versus Heterogeneous Oxide Iridium Electrocatalysts. *Journal of the American Chemical Society* **2022**, *144* (19), 8454–8459. <https://doi.org/10.1021/jacs.2c02006>.
- 43 Kwon, G.; Chang, S. H.; Heo, J. E.; Lee, K. J.; Kim, J. K.; Cho, B. G.; Koo, T. Y.; Kim, B. J.; Kim, C.; Lee, J. H.; Bak, S. M.; Beyer, K. A.; Zhong, H.; Koch, R. J.; Hwang, S.; Utschig, L. M.; Huang, X.; Hu, G.; Brudvig, G. W.; Tiede, D. M.; Kim, J. Experimental Verification of Ir 5d Orbital States and Atomic Structures in Highly Active Amorphous Iridium Oxide Catalysts. *ACS*

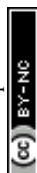


- Catalysis* **2021**, *11* (15), 10084–10094. <https://doi.org/10.1021/acscatal.1c00818>.
- 44 Kahk, J. M.; Poll, C. G.; Oropeza, F. E.; Ablett, J. M.; Céolin, D.; Rueff, J.-P.; Agrestini, S.; Utsumi, Y.; Tsuei, K. D.; Liao, Y. F.; Borgatti, F.; Panaccione, G.; Regoutz, A.; Egdell, R. G.; Morgan, B. J.; Scanlon, D. O.; Payne, D. J. Understanding the Electronic Structure of IrO<sub>2</sub> Using Hard-X-Ray Photoelectron Spectroscopy and Density-Functional Theory. *Phys. Rev. Lett.* **2014**, *112* (11), 117601. <https://doi.org/10.1103/PhysRevLett.112.117601>.
- 45 Yellowlees, L. J.; Macnamara, K. G. Iridium. In *Comprehensive Coordination Chemistry II*; 2003; Vol. 6, pp 147–246.
- 46 Crabtree, R., H. High Oxidation State Complexes of Rhodium and Iridium. In *Comprehensive Coordination Chemistry III*; 2021; pp 159–170.
- 47 Ooka, H.; Wang, Y.; Yamaguchi, A.; Hatakeyama, M.; Nakamura, S.; Hashimoto, K.; Nakamura, R. Legitimate Intermediates of Oxygen Evolution on Iridium Oxide Revealed by in Situ Electrochemical Evanescent Wave Spectroscopy. *Phys. Chem. Chem. Phys.* **2016**, *18* (22), 15199–15204. <https://doi.org/10.1039/C6CP02385A>.
- 48 Gottesfeld, S.; McIntyre, J. D. E.; Beni, G.; Shay, J. L. Electrochromism in Anodic Iridium Oxide Films. *Applied Physics Letters* **1978**, *33* (2), 208–210. <https://doi.org/10.1063/1.90277>.
- 49 Pavlovic, Z.; Ranjan, C.; Gao, Q.; Van Gastel, M.; Schlögl, R. Probing the Structure of a Water-Oxidizing Anodic Iridium Oxide Catalyst Using Raman Spectroscopy. *ACS Catal.* **2016**, *6* (12), 8098–8105. <https://doi.org/10.1021/acscatal.6b02343>.
- 50 Mo, Y.; Stefan, I. C.; Cai, W. B.; Dong, J.; Carey, P.; Scherson, D. A. In Situ Iridium LIII-Edge X-Ray Absorption and Surface Enhanced Raman Spectroscopy of Electrodeposited Iridium Oxide Films in Aqueous Electrolytes. *Journal of Physical Chemistry B* **2002**, *106* (14), 3681–3686. <https://doi.org/10.1021/jp014452p>.
- 51 Sasaki, Y.; Kato, H.; Kudo, A. [Co(bpy)<sub>3</sub>]<sup>3+/2+</sup> and [Co(phen)<sub>3</sub>]<sup>3+/2+</sup> Electron Mediators for Overall Water Splitting under Sunlight Irradiation Using Z-Scheme Photocatalyst System. *Journal of the American Chemical Society* **2013**, *135* (14), 5441–5449. <https://doi.org/10.1021/ja400238r>.
- 52 Douglas Dalzel Perrin. *Dissociation Constants of Inorganic Acids and Bases in Aqueous Solution*; Pergamon: New York, New York, 1982.
- 53 Awtrey, A. D.; Connick, R. E. The Absorption Spectra of I<sub>2</sub>, I<sub>3</sub><sup>-</sup>, I<sup>-</sup>, IO<sub>3</sub><sup>-</sup>, S<sub>4</sub>O<sub>6</sub><sup>2-</sup> and S<sub>2</sub>O<sub>3</sub><sup>2-</sup>. Heat of the Reaction I<sub>3</sub><sup>-</sup> = I<sub>2</sub> + I<sup>-</sup>. *J. Am. Chem. Soc.* **1951**, *73* (4), 1842–1843. <https://doi.org/10.1021/ja01148a504>.
- 54 Labasque, T.; Chaumery, C.; Aminot, A.; Kergoat, G. Spectrophotometric Winkler Determination of Dissolved Oxygen: Re-Examination of Critical Factors and Reliability. *Marine Chemistry* **2004**, *88* (1–2), 53–60. <https://doi.org/10.1016/j.marchem.2004.03.004>.
- 55 Yuen, M. F.; Lauks, I.; Dautremont-Smith, W. C. pH Dependent Voltammetry of Iridium Oxide Films. *Solid State Ionics* **1983**, *11* (1), 19–29. [https://doi.org/10.1016/0167-2738\(83\)90058-9](https://doi.org/10.1016/0167-2738(83)90058-9).
- 56 Fleischmann, S.; Mitchell, J. B.; Wang, R.; Zhan, C.; Jiang, D. E.; Presser, V.; Augustyn, V. Pseudocapacitance: From Fundamental Understanding to High Power Energy Storage Materials. *Chemical Reviews* **2020**, *120* (14), 6738–6782. <https://doi.org/10.1021/acs.chemrev.0c00170>.
- 57 Burke, L. D.; Twomey, T. A. M. Influence of Ph on the Redox Behaviour of Hydrous Nickel Oxide. *Journal of Electroanalytical Chemistry and Interfacial Electrochemistry* **1982**, *134* (2), 353–362. [https://doi.org/10.1016/0022-0728\(82\)80013-2](https://doi.org/10.1016/0022-0728(82)80013-2). View Article Online  
DOI: 10.1039/D6SC00492J
- 58 Bock, C.; Birss, V. I. Anion and Water Involvement in Hydrous Ir Oxide Redox Reactions in Acidic Solutions. *Journal of Electroanalytical Chemistry* **1999**, *475* (1), 20–27. [https://doi.org/10.1016/S0022-0728\(99\)00330-7](https://doi.org/10.1016/S0022-0728(99)00330-7).
- 59 Stoerzinger, K. A.; Rao, R. R.; Wang, X. R.; Hong, W. T.; Rouleau, C. M.; Shao-Horn, Y. The Role of Ru Redox in pH-Dependent Oxygen Evolution on Rutile Ruthenium Dioxide Surfaces. *Chem* **2017**, *2* (5), 668–675. <https://doi.org/10.1016/j.chempr.2017.04.001>.
- 60 Burke, L. D.; Whelan, D. P. A Voltammetric Investigation of the Charge Storage Reactions of Hydrous Iridium Oxide Layers. *Journal of Electroanalytical Chemistry and Interfacial Electrochemistry* **1984**, *162* (1–2), 121–141.
- 61 Kuo, D.-Y.; Kawasaki, J. K.; Nelson, J. N.; Kloppenburg, J.; Hautier, G.; Shen, K. M.; Schlom, D. G.; Suntivich, J. Influence of Surface Adsorption on the Oxygen Evolution Reaction on IrO<sub>2</sub> (110). *J. Am. Chem. Soc.* **2017**, *139* (9), 3473–3479. <https://doi.org/10.1021/jacs.6b11932>.
- 62 Petit, M. A.; Plichon, V. Anodic Electrodeposition of Iridium Oxide Films. *Journal of Electroanalytical Chemistry* **1998**, *444* (2), 247–252. [https://doi.org/10.1016/S0022-0728\(97\)00570-6](https://doi.org/10.1016/S0022-0728(97)00570-6).
- 63 Vanleugenhaghe, C.; Valensi, G.; Pourbaix, M. Pourbaix, M. Iodine. In *Atlas of Electrochemical Equilibria in Aqueous Solutions*; NACE International, 1974; pp 614–626.
- 64 Gileadi, E. Adsorption in Electrochemistry. In *Electrosorption*; Springer, 1967; pp 1–18.
- 65 Bard, A. J.; Faulkner, L. R. Double-Layer Structure and Adsorption. In *Electrochemical Methods: Fundamentals and Applications*; John Wiley & Sons, Inc., 2001; pp 534–579.
- 66 Delahay, P. *Double Layer and Electrode Kinetics*; Interscience Publishers, 1965.
- 67 Gileadi, E. *Electrode Kinetics for Chemists, Chemical Engineers, and Materials Scientists*; John Wiley & Sons, 1996. The discussion here, and the quoted text, are from pp. 262–266.
- 68 Norby, T.; Widerøe, M.; Glöckner, R.; Larring, Y. Hydrogen in Oxides. *Dalton Trans.* **2004**, No. 19, 3012–3018. <https://doi.org/10.1039/B403011G>.
- 69 Pourbaix, M. *Atlas of Electrochemical Equilibria in Aqueous Solutions*; National Association of Corrosion Engineers, 1974.
- 70 McCarthy, B. D.; Dempsey, J. L. Decoding Proton-Coupled Electron Transfer with Potential-pKa Diagrams. *Inorganic Chemistry* **2017**, *56* (3), 1225–1231. <https://doi.org/10.1021/acs.inorgchem.6b02325>.
- 71 Hu, B.; Kuo, D. Y.; Paik, H.; Schlom, D. G.; Suntivich, J. Enthalpy and Entropy of Oxygen Electroadsorption on RuO<sub>2</sub>(110) in Alkaline Media. *Journal of Chemical Physics* **2020**, *152* (9). <https://doi.org/10.1063/1.5139049>.
- 72 Grokipedia v2.0., [https://grokipedia.com/page/alexander\\_frumkin](https://grokipedia.com/page/alexander_frumkin), (accessed January 14, 2026)
- 73 Christmann, K. Interaction of Hydrogen with Solid Surfaces. *Surface Science Reports* **1988**, *9* (1–3), 1–163. [https://doi.org/10.1016/0167-5729\(88\)90009-X](https://doi.org/10.1016/0167-5729(88)90009-X).
- 74 Rizo, R.; Sitta, E.; Herrero, E.; Climent, V.; Feliu, J. M. Towards the Understanding of the Interfacial pH Scale at Pt(111) Electrodes. *Electrochimica Acta* **2015**, *162*, 138–145. <https://doi.org/10.1016/j.electacta.2015.01.069>.
- 75 Moss, B.; Svane, K. L.; Nieto-Castro, D.; Rao, R. R.; Scott, S. B.; Tseng, C.; Sachs, M.; Pennathur, A.; Liang, C.; Oldham, L. I.; Mazzolini, E.; Jurado, L.; Sankar, G.; Parry, S.; Celorrio, V.; Dawlaty, J. M.; Rossmeisl, J.; Galán-Mascarós, J. R.; Stephens,



- I. E. L.; Durrant, J. R. Cooperative Effects Drive Water Oxidation Catalysis in Cobalt Electrocatalysts through the Destabilization of Intermediates. *J. Am. Chem. Soc.* **2024**, *146* (13), 8915–8927. <https://doi.org/10.1021/jacs.3c11651>.
- 76 Gibson, N. J.; Parada, G. A.; Mercado, B. Q.; Mayer, J. M. Colloidal Hexagonal Tungsten Oxide Nanorods: Synthesis, Characterization, and Proton-Coupled Electron Transfer. *Inorg. Chem.* **2026**, *65* (4), 2659–2668. <https://doi.org/10.1021/acs.inorgchem.5c06029>.
- 77 González, D.; Sodupe, M.; Rodríguez-Santiago, L.; Solans-Monfort, X. Surface Morphology Controls Water Dissociation on Hydrated IrO<sub>2</sub> nanoparticles. *Nanoscale* **2021**, *13* (34), 14480–14489. <https://doi.org/10.1039/d1nr03592d>.
- 78 Mu, R.; Cantu, D. C.; Lin, X.; Glezakou, V. A.; Wang, Z.; Lyubinetsky, I.; Rousseau, R.; Dohnálek, Z. Dimerization Induced Deprotonation of Water on RuO<sub>2</sub>(110). *Journal of Physical Chemistry Letters* **2014**, *5* (19), 3445–3450. <https://doi.org/10.1021/jz501810g>.
- 79 Hill, A. G.; Castillo, M. C.; Bacsa, J.; Otte, K. S.; Soper, J. D. Redox-Active Ligands Permit Multielectron O<sub>2</sub> Homolysis and O-Atom Transfer at Exceptionally High-Valent Vanadyl Complexes. *Journal of the American Chemical Society* **2025**, *147* (16), 13356–13369. <https://doi.org/10.1021/jacs.4c18305>.
- 80 Holm, R. H.; Donahue, J. P. A Thermodynamic Scale for Oxygen Atom Transfer Reactions. *Polyhedron* **1993**, *12*, 571–589.
- 81 Ellingham, H. J. T. Transactions and Communications. *J. Chem. Technol. Biotechnol.* **1944**, *63* (5), 125–160. <https://doi.org/10.1002/jctb.5000630501>.
- 82 Rai, R.; Li, T.; Liang, Z.; Kim, M.; Asthagiri, A.; Weaver, J. F. Growth and Termination of a Rutile IrO<sub>2</sub>(100) Layer on Ir(111). *Surface Science* **2016**, *652*, 213–221. <https://doi.org/10.1016/j.susc.2016.01.018>.

View Article Online  
DOI: 10.1039/D6SC00492J



The datasets supporting this article have been uploaded as part of the Electronic Supplementary Information.

